

Insight into tetracycline photocatalytic degradation mechanism in a wide pH range on BiOI/BiOBr: Coupling DFT/QSAR simulations with experiments



Qianqian Ni ^a, Xin Ke ^{a,*}, Wenjing Qian ^a, Zheng Yan ^a, Jingde Luan ^a, Wengang Liu ^b

^a Liaoning Key Laboratory of Clean Energy and College of Energy and Environmental, Shenyang Aerospace University, 110136, Shenyang, China

^b School of Resources and Civil Engineering, Northeastern University, 11 Wenhua Road, Heping District, Shenyang 110819, China

ARTICLE INFO

Keywords:
Photocatalysis
Tetracycline
Deprotonation
Wide pH
Density functional theory

ABSTRACT

A single hydrothermal reaction was used to create BiOI/BiOBr composites, which demonstrated good sunlight-driven photocatalytic degradation activity of tetracycline (TC) over a broad pH range and the degradation efficiency can be stable at about 90%. Moreover, $\cdot\text{O}_2$ has been identified as the most important active ingredient in the photocatalytic system. Density functional theory (DFT) calculations were used to investigate the electron transfer mechanism of BiOX heterojunctions on a molecular scale, as well as to propose possible photocatalytic degradation mechanisms and reaction sites for tetracycline in different deprotonated forms at a wide range of pH values. The quantitative structure-activity relationship (QSAR) was also used to assess the toxicity of the intermediates. In summary, this study presents new concepts for investigating the photodegradation behavior of antibiotics throughout a wide pH range, which is predicted to be employed for surface water remediation.

1. Introduction

Antibiotics have long been used to treat infectious illnesses in people and livestock, as well as to enhance animal development. Yet, antibiotic misuse has had negative environmental consequences and constitutes a significant hazard to humans and microbes [1]. TC is one of the most often used antibiotics in aquaculture and veterinary care due to its low cost and potent antibacterial properties [2–5]. Yet, due to the presence of numerous functional groups, pH is one of the variables influencing TC stability in solution [6]. As a result, how to efficiently and stably remove TC across a wide variety of pH settings in conjunction with TC's inherent qualities is an essential and urgent topic.

Photocatalytic, physical adsorption, and biochemical treatment methods have been developed in recent years to successfully breakdown TC in the environment [2,7,8]. Among these, semiconductor-based photocatalysis has a considerable competitive advantage since it directly degrades TC using solar light [2,4,9,10]. Similarly, several studies have shown that pH is a crucial factor influencing photocatalytic performance [11–13]. The ideal pH of semiconductor photocatalysts is often confined to a small range. For example, the ideal pH for the breakdown of amoxicillin in aqueous solution for the typical photocatalyst ZnO photocatalyst is 11 [14]. The ideal working pH of TiO₂ in

aniline chloride degradation is 9.0 [15]. Outside of this limited pH range, catalytic efficiency suffers greatly. Therefore, photocatalysts that can stabilize tetracycline degradation over the whole pH range must be developed.

There are numerous photocatalytic materials available today, including bismuth halide oxide BiOX (X = Cl, Br, I) with a layered structure, which ensures excellent photocatalytic activity due to their two-dimensional crystal structure, induced internal electric field (IEF), and indirect band gap to inhibit electron-hole complexation [16,17]. However, the pure-phase BiOX, is physically constrained by strong Coulomb force interactions between electron-hole pairs in its $[\text{Bi}_2\text{O}_2]^{2+}$ flat plate, which can result in exciton effects. The exciton creation will compete with the generation of free carriers, which dramatically influences the photocatalytic efficiency [18]. Many efforts are being made to promote the dissociation of excitons into free carriers, one of which is the construction of heterojunctions, which can change the charged edge into disordered edges, particularly near the interface, thereby promoting exciton dissociation and enhancing charge carrier-dominated photocatalytic reactions [19–23].

It has been demonstrated that the heterojunction-modified pure-phase BiOX may be designed to have higher negative conduction band potentials and interact with electrons to produce more superoxide

* Corresponding author.

E-mail address: kex@iae.ac.cn (X. Ke).

radicals [22,24]. In a wide pH range, the degradation of some of the active substances can also be weakened due to environmental influences. For example, too much OH⁻ was discovered to react with photogenerated cavities, producing too much ·OH and so preventing direct cavity oxidation. While acidic circumstances encourage the synthesis of HO₂ from O₂[·], which is a precursor of H₂O₂ and ·OH, alkaline conditions do not [25–27]. Based on this, one can begin by considering how to develop adequate active compounds in order to ensure effective tetracycline breakdown throughout a wide pH range. Because ·OH is quickly impacted by ambient pH and cannot guarantee its activity over a large pH range, enriching additional radicals such as O₂[·] and h⁺ can provide efficient tetracycline breakdown over a wide pH range [28–32]. In turn, superoxide radical enrichment may be accomplished by altering the location of the conduction band structure while developing the material. In brief, the heterojunction was built to change the energy band structure of BiOX, change the band edge position, enrich O₂[·], and inhibit the production of ·OH, thereby eliminating the negative impact of ·OH's insufficient ability to degrade pollutants over a wide pH range and allowing BiOX to efficiently degrade tetracycline over a wide pH range.

To summarize, in this study, firstly, the BiOI/BiOBr composite material that can directionally regulate O₂[·] production was synthesized by hydrothermal synthesis to construct the heterojunction structure of efficient carrier separation. Through the study of front-end photocatalytic materials, the mechanism of BiOX heterojunction stable degradation of TC at high pH value was discussed. Analytical techniques were used to analyze the morphology, composition, and structure of the produced samples, and density generalization calculations were used to investigate the electron transfer transitions at the heterojunction interface and the corresponding energy band features. The toxicity of the intermediate after conventional degradation was reasonably predicted by combining with LC-MS detection and toxicological analysis, and the properties of tetracycline were investigated at the molecular scale for the back-end contaminant tetracycline under different pH conditions. The ultimate goal is to elucidate the mechanism underlying the stable degradation of tetracycline by BiOX heterostructures over a wide pH range, and it is hoped that these findings will inspire further research into the stable degradation of tetracycline antibiotic wastewater by photocatalysts at various pH levels.

2. Materials and methods

2.1. Chemicals

Potassium bromide (KBr), potassium iodide (KI), ethylene glycol ((CH₂OH)₂), disodium ethylenediaminetetraacetate (EDTA-2Na), isopropyl alcohol (IPA), and p-benzoquinone (BQ) were purchased from Aladdin Biochemical Co. Bismuth nitrate pentahydrate Bi(NO₃)₃·5 H₂O was purchased from McLean Biochemical Co. All chemicals were of analytical grade and used without further purification.

2.2. Materials preparation

Add 40 mL of ethylene glycol into a beaker, weigh 16 mmol of Bi(NO₃)₃·5H₂O into it, and obtain a homogeneous mixed solution by sonication and magnetic stirring, then add 0.2720 g of KBr to the mixed solution, stir magnetically until homogeneous, and continue stirring to add 2.2766 g (nKBr:nKI=1:6) of KI (The total amount of KBr and KI added was set to 16 mmol) and 20 mL of Wahaha water, and the homogeneous solution was obtained by stirring for 20 min. The mixed homogeneous solution was then put into the liner of a 100 mL reaction kettle and the hydrothermal reaction was carried out at 140 °C for 8 h. After the reaction, it was washed by centrifugation with deionized water and anhydrous ethanol alternately three times and collected by freeze-drying at -40 °C for 12 h. Other products with ratios of 1:3, 1:4 and 1:8 could be obtained using the same method. In contrast, BiOI and

BiOBr were prepared by simply adding KI or KBr (16 mmol) on top of the above method.

2.3. Materials characterization

The crystal structure of the prepared samples was characterized by X-ray powder diffraction (XRD). The surface morphology and elemental distribution of the obtained photocatalysts were determined by transmission electron microscopy (TEM) equipped with an energy dispersive X-ray spectrometer (EDS). The elemental composition and energy binding state of the elements are analyzed by X-ray photoelectron spectroscopy (XPS). Material-to-material agreement is analyzed by external spectral detection analysis (FTIR). The optical absorption properties of the synthesized samples are characterized by UV-Vis diffuse reflectance spectroscopy (DRS), and the charge transfer properties are characterized by photoluminescence (PL) spectroscopy, electrochemical impedance spectroscopy (EIS), and photocurrent (PC) response. A 3-electrode electrochemical analysis approach was used to evaluate photocurrent (PC) and electrochemical impedance spectroscopy (EIS) using a CHI 660E electrochemical workstation. Working electrodes, counter electrodes, and reference electrodes were made using synthesized samples, Pt sheets, and Hg/HgCl, respectively. Before testing, the samples were ultrasonically disseminated in anhydrous ethanol. The electrolyte was a solution of 0.1 M Na₂SO₄. Light/dark short-circuit photocurrents were measured with a 300 W xenon lamp (> 420 nm) and an open-circuit voltage as bias. All experimental parameters, including temperature and distance between the light source and the reaction solution, were kept constant to guarantee repeatability. The LC-MS analysis was carried out in both positive and negative electrospray ionization modes ESI(-)(+). Tetracycline and its intermediates have mass-to-charge ratios (*m/z*) in the 50–750 range. At a flow rate of 0.5 mL/min, the injection volume was 2 μL, and the mobile phases were 30% formic acid (0.1%) and 70% methanol.

2.4. Photocatalytic experiment

The photocatalytic activity of the prepared samples was evaluated by degrading the TC in simulated solar radiation. A 300 W xenon lamp (CEL-HXF300-T3) was used as the light source. Prior to photocatalytic degradation, 0.06 g of photocatalyst was added to 160 mL of TC solution (10 mg/L, pH = 8.5) and stirred at 670 rpm in the dark for 30 min to reach adsorption-desorption equilibrium. Photodegradation experiments were then started by exposing the photoreactor to simulated sunlight. Every 10 min, 5 mL of the solution was removed from the photoreactor and filtered through a 0.22 μm nylon syringe filter and analyzed for TC concentration using a UV spectrophotometer at 357 nm. TC degradation data were fitted by a secondary kinetic law and the best-fit kinetics (k) were calculated for the BiOI and BiOBr composites.

The contribution of various reactive substances, namely superoxide (O₂[·]), hydroxyl group (·OH) and hole (h⁺), to the photocatalytic degradation of TC was evaluated by applying selective radical scavengers. Specifically, disodium ethylenediaminetetraacetate (EDTA-2Na, 50 mM), p-benzoquinone (BQ, 50 mM) and isopropyl alcohol (IPA, 50 mM) were chosen as O₂[·], h⁺ and ·OH scavengers.

2.5. DFT calculation and toxicity evaluation

The calculations in this study make use of the PBE and GGA generalized functions for geometry optimization and associated simulations, as well as the CASTEP and DMol3 codes from Materials Studio for density generalized function theory calculations for materials and contaminants, respectively. The K-point is Quality, the SCF tolerance is 1.0×10^{-5} eV/Å, the maximum force on the atom is 0.05 eV/Å, and the energy cutoff for the plane wave expansion is 500 eV for the geometry optimization. The important calculations for the composite material are the differential charge density, the corresponding energy band structure,

the frontier orbitals, the electrostatic potential, and the Fukui function of the contaminant. Using the toxicity estimating software tool (T.E.S.T.) and quantitative constitutive relationships (QSAR), the toxicity of intermediates in the degradation pathway of the pollutants was also simulated.

3. Results and discussion

3.1. Photoactivity performance

For the photocatalytic performance of the composites, the photocatalytic degradation rate of TC with time under visible light was used to evaluate the photocatalytic performance of the samples (see Eq. 1), and we also took into account the effect of the optical properties of the catalyst itself (e.g., optical thickness) (Text S1) to find the optimal optical thickness by varying the amount of the additive, which ultimately led to the insight into the photocatalytic degradation mechanisms of tetracycline over a wide pH range for BiOI /BiOBr.

$$\eta_{TC} = \frac{C_0 - C_t}{C_0} \times 100\% \quad (1)$$

Where η_{TC} is the removal efficiency (%), C_0 is the initial concentration of TC, mg/L, C_t is the measured concentration of TC at time t , mg/L.

When the pure phases of BiOBr and BiOI were put in TC solution under dark circumstances, the adsorption equilibrium was attained after 30 min with adsorption efficiencies of 2.17% and 42.99%, respectively. The ultimate degradation efficiencies of BiOBr and BiOI were 54.83%

and 86.83%, respectively, when the light source was turned on. Although the results are not especially promising, it is evident that BiOI outperforms BiOBr in terms of degrading performance. To boost photodegradability, composites can be made by mixing BiOI with pure-phase BiOBr. On this premise, it was discovered that when varied ratios of composite catalysts were added into the TC solution, the addition of varying ratios of BiOI to BiOBr lowered the TC concentration on these materials by roughly 25%–47%. After 30 min of adsorption equilibrium, the photocatalytic destruction of TC was performed under visible light irradiation at a wavelength larger than 400 nm. The BB-6 photocatalyst demonstrated good photocatalytic activity during the photocatalytic process. After 90 min of response, the TC degradation efficiency was 91.92%. BB-6 not only has high photodegradation ability, but also has exceptional front-end adsorption capacity, which is approximately 20 times that of pure-phase BiOBr. The photocatalytic destruction of the pollutant is plainly seen in the overall process.

The optimum optical thickness exploration performed later is shown in Fig. 1(b), where BB-6 was used as the target catalyst to go through the effect of the dosage on the degradation rate, while at the same time, according to the optical thickness theory [33–35], it can be seen that the dosage will have an effect on the optical thickness by fixing the depth of the reactor, and thus the degradation efficiency may be affected by the optical properties. According to the Fig. 1(b), increasing the catalyst dose from 0.2 g/L to 0.5 g/L resulted in an improvement in total degrading efficiency within 90 min of the light being switched on, which were 87.27%, 90.61%, 92.12%, and 93.03%, respectively. Catalyst optical thicknesses were 0.17, 0.26, 0.34, and 0.43. Based on the results,

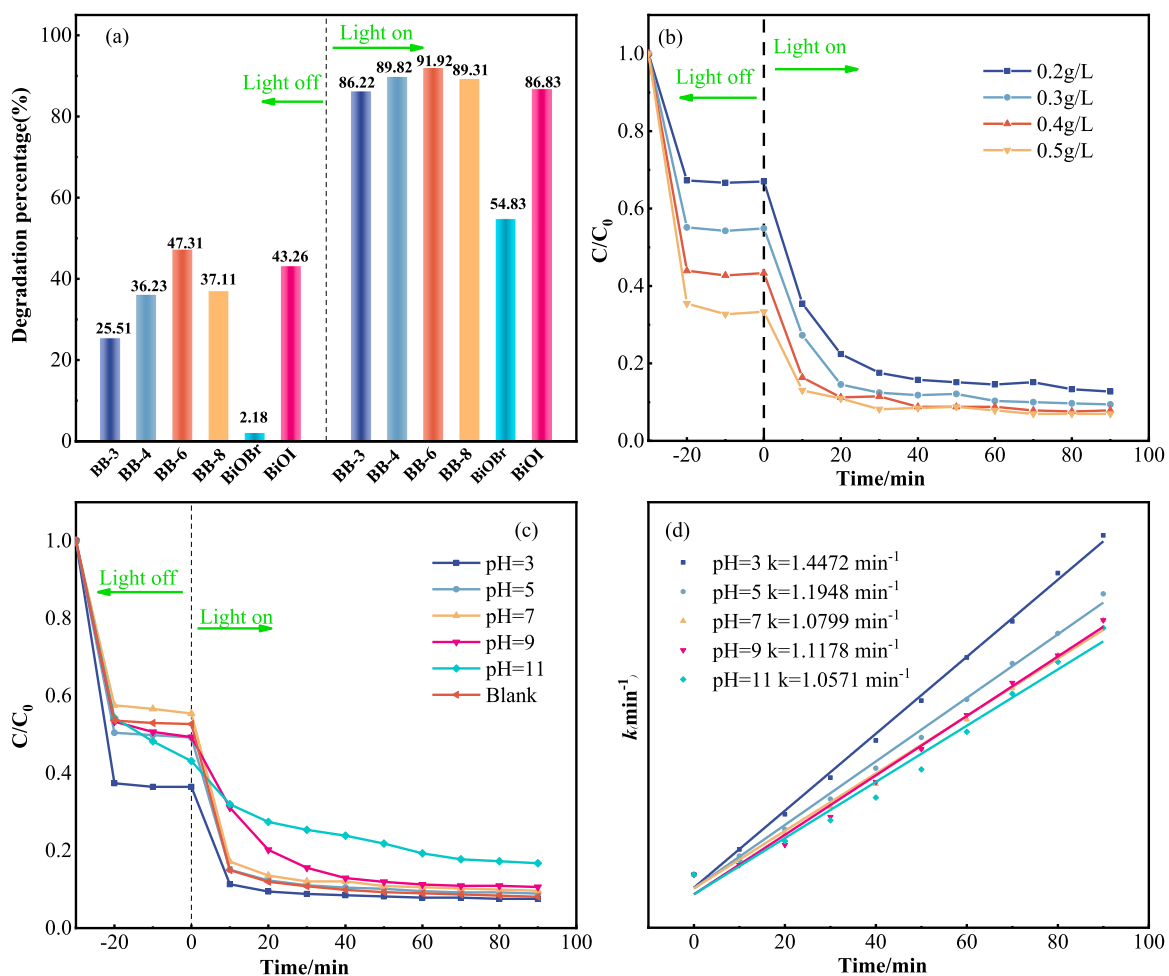


Fig. 1. (a) The summary of adsorption situation in dark and degradation performance after simulated solar light irradiation of 90 min; (b) Dosage situation; (c) Degradation efficiency of TC under different pH conditions; (d) Kinetic constants at different pH conditions.

0.4 g/L was chosen as the catalyst dose for the further studies, taking into account both the degrading efficiency and the optical thickness. This maintains the degrading efficiency at around 90% and minimizes energy consumption owing to the rise in optical thickness, ensuring a certain economy.

Fig. 1(c)-(d) evaluated the degrading impact of BB-6 on TC at pH 3, 5, 7, 9, and 11 after identifying the best settings. The rate of degradation can be seen more clearly through the reaction rate constants (**Eq.2**). It was discovered that BB-6 retained its outstanding breakdown ability at various pH levels. The results demonstrated that changing the pH value had no effect on BB-6's overall photocatalytic degradation capacity, and the degradation rate of TC could still be managed at around 90%. This demonstrates that BB-6 has great degrading ability as well as high stability. The related kinetic constants are shown in **Fig. 1(d)**, and it can be seen that the degradation efficiency of TC is much reduced at pH = 11. This might be because tetracycline is selective and is impeded when the environment is overly alkaline, resulting in tetracycline degradation efficiency being worse rather than better [2,36]. To further understand the influence of pH on tetracycline breakdown, blank trials at each pH value were compared (Fig.S1). The points in blue boxes reflect the initial readings after adjusting the pH of the tetracycline, after which it was consistent with typical experimental settings. Tetracycline is susceptible to breakdown at strong bases due to pH, however its degradation efficiency is substantially lower than when the catalyst is present. When multiple versions of tetracycline with differing pH values are combined, the catalyst can efficiently breakdown them. The impact of pH on tetracycline will be examined further in **Section 3.5** on a molecular level. To sum up, BB-6 has high photodegradation ability and great stability to sustain effective degradation efficiency throughout a wide pH range. To facilitate the comparison of effects, we have listed the relevant tables (Tab.S6).

$$\frac{t}{q_t} = \frac{1}{kq_e^2} + \frac{t}{q_e} \quad (2)$$

Where q_e and q_t are the quantities at equilibrium and time t , respectively (mg/L); t is the time (min).

3.2. Structure and morphology analysis

The XRD spectra indicate the crystal structures, phase purity, and composition of BiOI, BiOBr, and BB-6. The pure phase BiOI contains four unique diffraction peaks corresponding to (102), (110), (104), and (212), as illustrated in **Fig. 2(a)**, which are consistent with the tetragonal BiOI standard card (JCPDS No. 10-0445). Similarly, in the pure phase BiOBr, seven different diffraction peaks can be detected, (001), (101), (110), (102), (112), (200), (104), (212), and (310), which are in agreement with the

tetragonal BiOBr standard card (JCPDS 09-0393), and their clear peak forms imply their excellent crystallinity. XRD diffraction peaks corresponding to BiOI and BiOBr may be clearly seen in the BB-6 nanomaterial. The diffraction peaks with $2\theta = 29.8^\circ, 45.5^\circ, 55.3^\circ, 22.3^\circ$, and 31.8° correspond to BiOI (102), (110), (104) and BiOBr (101), respectively (102). Furthermore, the distinctive peaks of BiOI are more visible in the composites, owing to the increased presence of BiOI compared to BiOBr. Moreover, no further spurious peaks emerge in the composite plots, indicating that no contaminants were introduced during the synthesis process.

The functional groups of BiOI, BiOBr, and BB-6 were then investigated using FT-IR spectroscopy. FT-IR spectroscopy was used to investigate the functional groups of BiOI, BiOBr, and BB-6. The usual bands at 510 cm^{-1} and 503 cm^{-1} for BiOI and BiOBr, as illustrated in **Fig. 2(b)**, can be ascribed to the stretching vibration of Bi-O [37]. While the large peak bands at 3380 cm^{-1} and 3447 cm^{-1} for both can be attributable to the adsorbed water molecules' O-H stretching and O-H bending vibrations [38]. All of the distinctive peaks of BiOI and BiOBr are substantially retained in the nanocomposite BB-6. Furthermore, the composites exhibit a minor shift in the Bi-O and O-H stretching vibrational bands when compared to the two pure phase materials, indicating that there is an interaction between BiOBr and BiOI. The following results show that the synthesis of BiOI/BiOBr composites was effective and that BiOBr has a cross-linking action with BiOI rather than simple mechanical mixing.

SEM was used to examine the morphologies of synthesized BB-6, BiOI, and BiOBr. BiOI and BiOBr have two-dimensional lamellar and three-dimensional spherical structures, respectively, and excellent crystallinity, as shown in **Fig. 3(b)-(c)**. The sheet-like BiOI is wrapped around the spherical BiOBr in the BB-6 nanocomposite (**Fig. 3(a)**), causing the BiOBr structure to become sparse and blooming, resulting in a flowering spherical structure. The EDS mapping was then used to characterize the distribution of the various elements on the nanomaterials' surfaces (**Fig. 3(d)**). Elements I, Br, Bi, and O are represented by cyan, red, purple, and green, respectively, which is consistent with the XPS results. The uniform distribution of numerous components on the photocatalyst surface demonstrates that the nanomaterials were successfully synthesized.

Besides that, TEM characterization was carried out to investigate the positional connection between BiOI and BiOBr in BB-6 further. Combining BiOI with BiOBr results in a tight and dense heterojunction interface, as seen in **Fig. 4**. The creation of heterojunctions typically enhances electron transport and electron-hole pair separation efficiency. HRTEM (**Fig. 4(b)-(c)**) reveals typical lattices of 0.28 nm, corresponding to BiOBr and BiOI, respectively [39,40]. Based on the findings, it was determined that a heterojunction created by BiOI and BiOBr was effectively produced, which increased photoelectron transport.

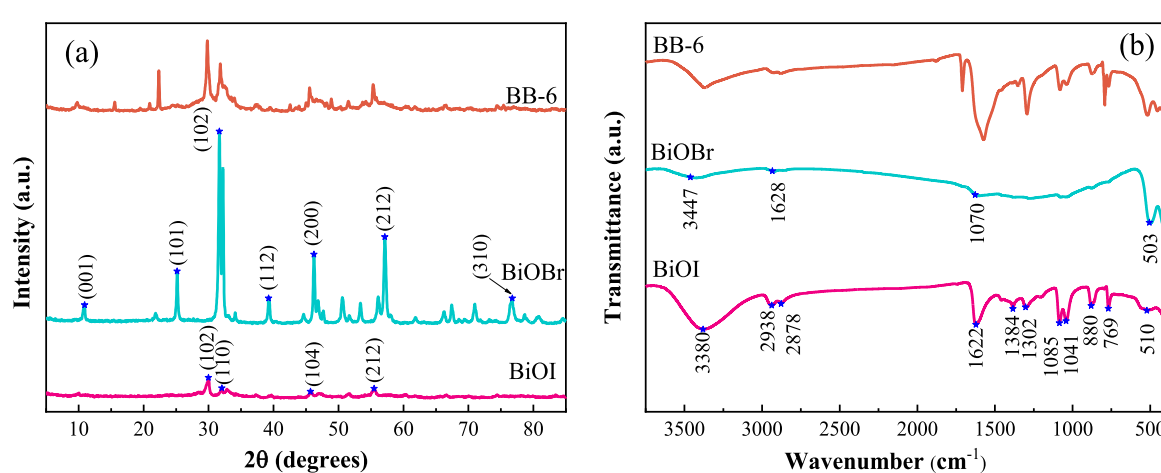


Fig. 2. (a) XRD patterns and (b) FT-IR spectra of the as-prepared BiOI, BiOBr and BB-6.

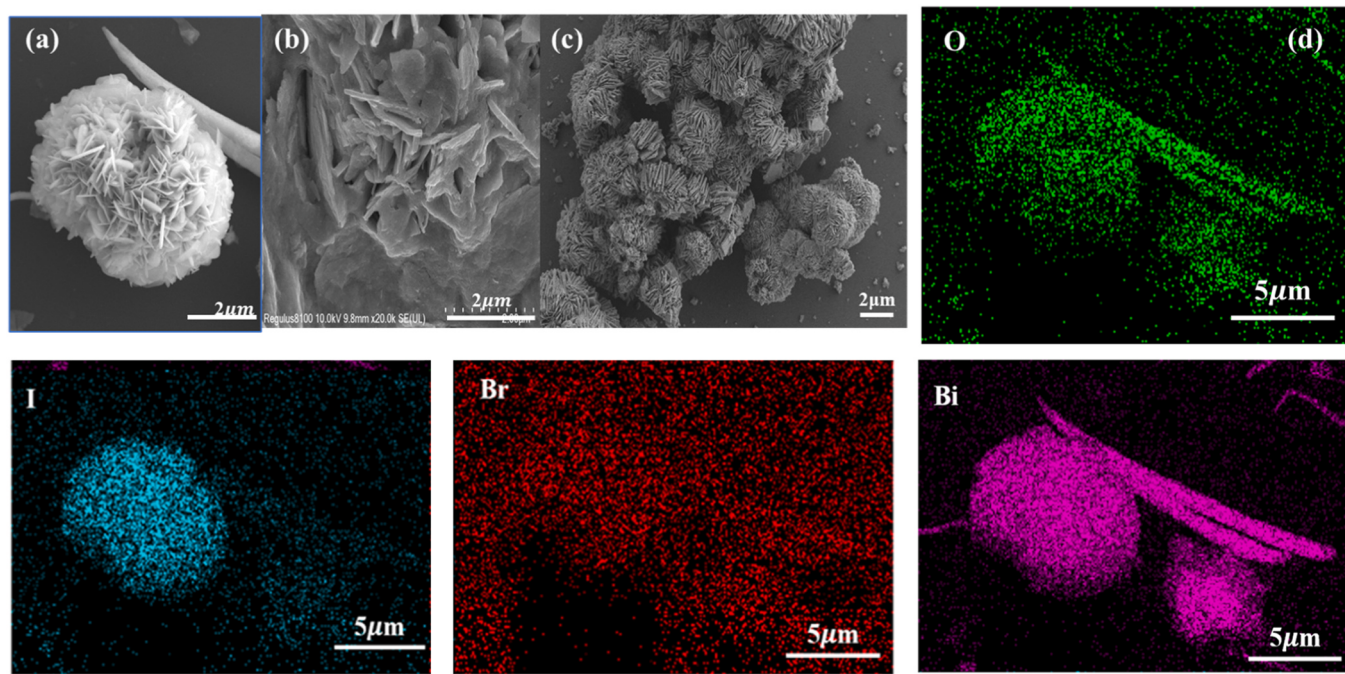


Fig. 3. SEM images of the as-prepared (a) BB-6, (b) BiOI, and (c) BiOBr. (d) EDS mappings of BB-6.

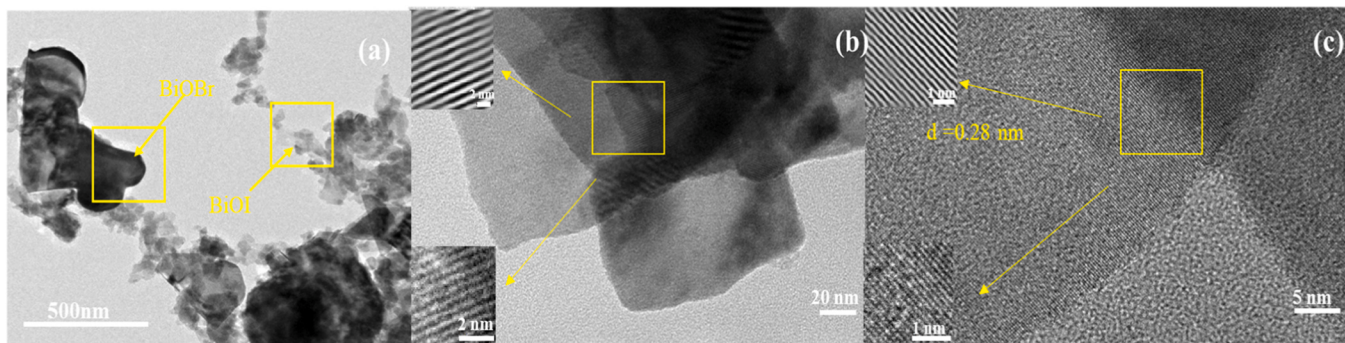


Fig. 4. TEM (a) and HRTEM (b-c) images of BB-6.

XPS measurements were conducted to study the elemental makeup and binding locations of the samples. The presence of five elements, C 1 s, O 1 s, Bi 4 f, Br 3d, and I 3d, mostly from BB-6, is confirmed by the XPS picture in Fig. 5(a), which is compatible with the EDS mapping results. The C 1 s spectra is separated into two distinct peaks at binding energies of 284.8 eV and 288.41 eV, which are attributed to the sp² linked carbon (C-C bond) and during the reaction, part of the ester group residue of ethylene glycol oxidation (C=O bond), respectively, as shown in Fig. 5(b) [41,42]. The high resolution O 1 s spectra was fitted to Fig. 5(c) with distinctive peaks of 530.03 eV and 531.47 eV, respectively, belonging to the oxygen monomer and Bi-O groups adsorbed on the surface of the composite BB-6. In Fig. 5(d), two peaks are ascribed to Bi 4 f_{7/2} and Bi 4 f_{5/2}, which correspond to Bi³⁺ in BiOI and BiOBr, respectively [43]. 68.82 eV is assigned to Br 3d_{3/2} (Fig. 4(e)). Peaks at 630.45 and 619.01 eV are assigned to I 3d_{5/2} and I 3d_{7/2}, respectively (Fig. 5(f)). As a result, the XPS data support the effective synthesis of BiOI/BiOBr nanocomposites.

3.3. Band structure and optical absorption properties of materials

UV-Vis diffuse reflectance spectroscopy (DRS) analysis was used to analyze the light absorption characteristics of the resultant materials. The strong absorption bands of the pure phases BiOI and BiOBr are

approximately 200–500 nm and 200–450 nm, respectively, as shown in Fig. 6(a), whereas the particular optical absorption edges are displayed at 773 nm and 644 nm, respectively. BiOI has a very high visible light response and a wider visible light response range, according to the data. BiOBr, on the other hand, has a somewhat lower visible light capacity than BiOI. This might be attributable to the fact that removing monomeric Br from the surface changes the material's visible light response [44]. When the two are combined, their binary composite BB-6 exhibits an absorption edge at 732 nm that is blue-shifted compared to BiOI and red-shifted compared to BiOBr, suggesting that the composite can widen the visible response range due to the higher photoresponsiveness and absorbing capabilities of BiOI.

The photocatalytic process is determined by the energy band and electrical structure of the individual component semiconductors in photocatalysts. As a result, the band gaps of BiOI and BiOBr are found using UV-vis DRS spectra, and the band gap energy (E_g) of the samples is estimated using Kubelka-Munk (Eq. 3), whilst the valence band (VB) is determined using XPS-VB maps.

$$\alpha h\nu = A(h\nu - E_g)^n/2 \quad (3)$$

where α , h , ν , E_g , and A are the absorption coefficient, Planck's constant, light frequency, and band gap, respectively. The index n depends on the

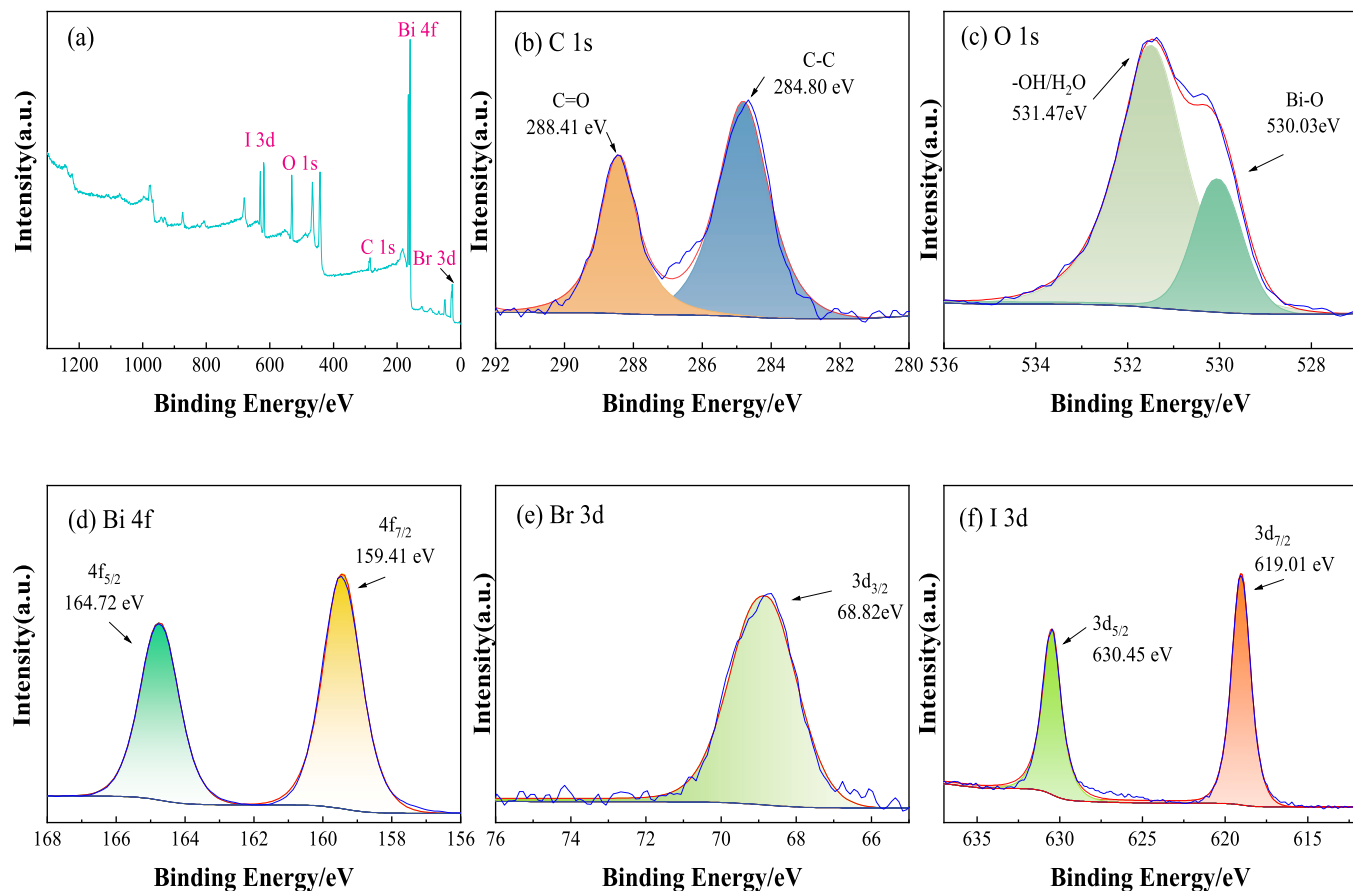


Fig. 5. XPS survey spectra (a) of BB-6. The comparison of high-resolution spectra of (b) C 1 s (c) O 1 s (c) Bi 4 f (d)Br 3d and (f) I 3d.

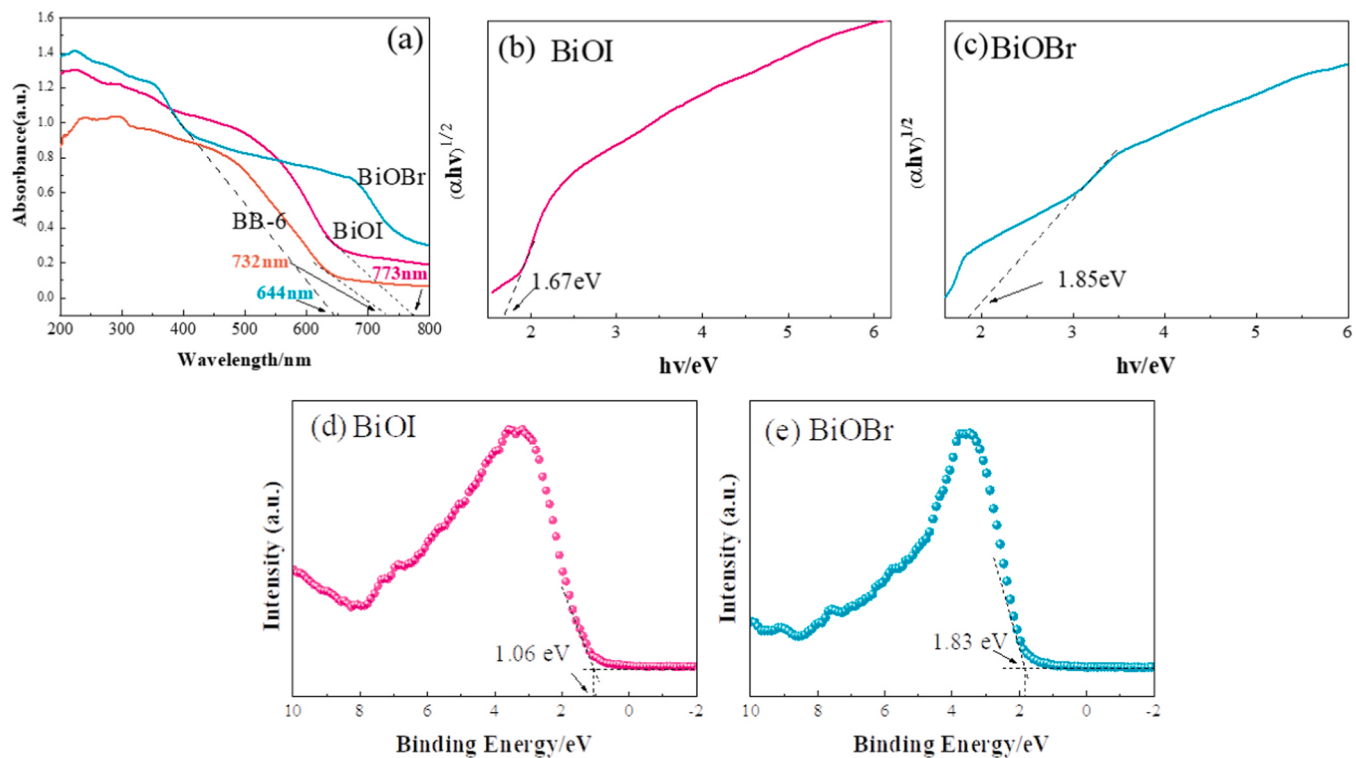


Fig. 6. (a) UV-vis absorption of the as-prepared BiOI, BiOBr and BB-6 samples. (b)-(c) Tauc plots of BiOI and BiOBr. (d)-(e) VB-XPS spectra of BiOI and BiOBr.

characteristics of the transition in a semiconductor, direct transition ($n = 1$) or indirect transition ($n = 4$) [1].

The band gaps of BiOI and BiOBr are 1.67 eV and 1.85 eV, respectively, as calculated from the distances between the CB and VB locations in Fig. 6(b)-(c) [45]. XPS-VB data were then used to describe the valence bands. As a result, the VB values of BiOI and BiOBr were discovered to be 1.06 eV and 1.83 eV, accordingly. (The calculation method is shown in Eq. 4). The CB values of BiOI and BiOBr may be determined to be -0.61 eV and -0.02 eV, respectively.

$$E_g = E_{VB} - E_{CB} \quad (4)$$

Depending on this, the potential degradation process was studied and analyzed further. For starters, the photogenerated electrons and holes of photocatalysts are readily compounded, limiting the photocatalysts' capacity to destroy contaminants. As a result, an

electrochemical workstation was used to conduct a more extensive photoelectrochemical performance examination of the composites. The composites' photoluminescence spectra (PL), transient photocurrent response (PC), and impedance (EIS) were all included. The peak emission intensity of BiOBr is the greatest in Fig. 7(a), suggesting the quickest electron-hole complexation rate. That explains why BiOBr has weak photocatalytic activity in the TC photodegradation process. When the two are joined, the PL value of the composite is much weaker than BiOBr and BiOI, showing that the electron-hole complexation is inhibited when BiOBr and BiOI form a heterojunction. Fig. 7(b)-(c) depicts the transient photocurrent density curves of BiOI, BiOBr, and BB-6 after eight irradiation cycles. All three samples had a consistent photocurrent response. BiOBr has the greatest arc radius and the lowest PC intensity, indicating a poor electron-hole separation efficiency. BB-6 has the lowest arc radius and the highest PC intensity, suggesting that it has a high efficiency of electron-hole separation. Indicating that the building of the BB-6

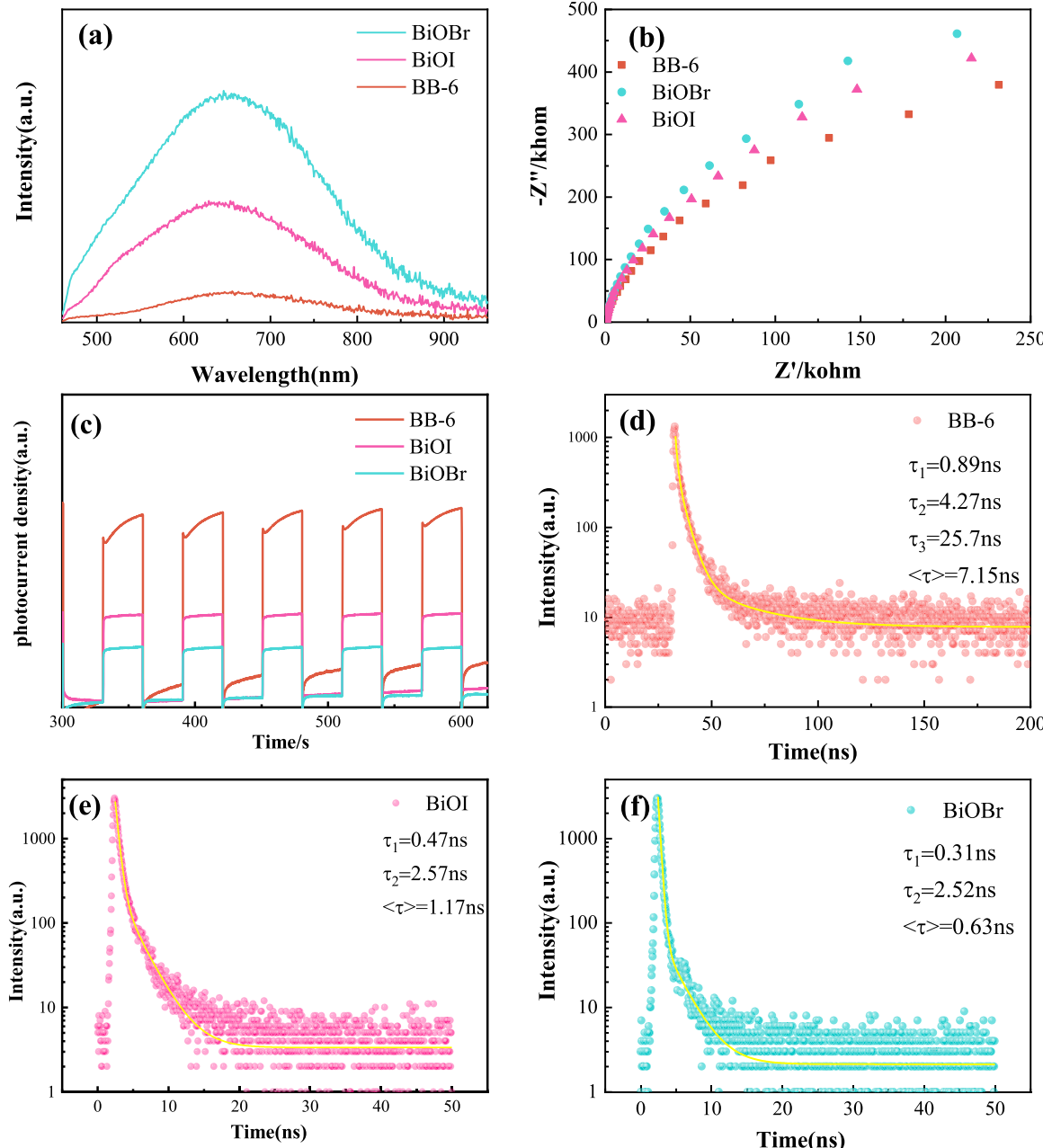


Fig. 7. The photoluminescence spectra (a) of BiOI, BiOBr and BB-6. (b) EIS spectra. (c) The transient photocurrent response of BiOI, BiOBr and BB-6. (d) TRPL spectra of BB-6. (e) TRPL spectra of BiOI. (f) TRPL spectra of BiOBr.

heterojunction between BiOI and BiOBr is favorable to the separation of electron-hole pairs. These three characterizations show that the development of heterogeneous structures improves charge separation and migration, hence enhancing the photocatalytic activity of the composites. To better highlight the carriers' key kinetic properties. The ns-level time-resolved photoluminescence spectra of pure BiOI, BiOBr, and BB-6 were also studied. The fluorescence lifetime data in Fig. 7(d)-(e) may be represented using Eq. (5). The prolonged fluorescence lifespan is related to the exciton's radiative complexation process from excited to ground state[46]. BB-6 has a longer lifespan than BiOI and BiOBr, indicating a considerable difference in carrier relaxation in the two states. Eq. (6) may also be used to compute the average fluorescence lifetime. According to the findings, the average fluorescence lifetimes of BiOI, BiOBr, and BB-6 are 1.17, 0.63, and 7.15 ns, respectively. The average fluorescence lifetime of BB-6 is much longer than that of BiOI and BiOBr, indicating that the heterojunction structure promotes exciton dissociation, which means that the photo-generated carriers have better separation and migration properties, promoting the photocatalytic process.

$$y(t) = y_0 + B_1 \exp(-t/\tau_1) + B_2 \exp(-t/\tau_2) + B_3 \exp(-t/\tau_3) \quad (5)$$

$$\langle \tau \rangle = \frac{B_1 \tau_1^2 + B_2 \tau_2^2 + B_3 \tau_3^2}{B_1 \tau_1 + B_2 \tau_2 + B_3 \tau_3} \quad (6)$$

Following that, radical capture tests were utilized to determine active radicals, and 50 mM IPA, BQ, and EDTA-2Na were used for scavenging studies of $\cdot\text{OH}$, h^+ , and $\cdot\text{O}_2^-$, respectively. If a considerable increase in degradation rate occurs after trapping a specific active substance compared to the blank group (equivalent to a higher column than the blank group), then this active substance plays a significant role in the photodegradation process. To illustrate the results more clearly, the bar graph in Fig. 8(a) shows that the combination of BQ and EDTA-2Na

resulted in a considerable decrease in the degradation rate of TC. Even while the addition of IPA reduces the degrading efficiency of TC somewhat, it is still not significantly different from the control trial. According to the results of radical capture tests, h^+ and $\cdot\text{O}_2^-$ radicals are the most active radicals, whereas $\cdot\text{OH}$ radicals have a smaller influence on photocatalytic degradation. To establish the active species, ESR, NBT, or TA-PL analysis is commonly employed to confirm the production of free radicals [47,48]. ESR spin capture spectroscopy with DMPO as trapping agents was used to confirm the existence of reactive oxygen species (ROS) in the photocatalytic process [49,50]. According to the ESR data, after turning on the light, a distinct signal of superoxide radicals developed, but the signal of hydroxyl radicals remained unchanged. The active chemicals were superoxide radicals and cavities, as in earlier capture studies. The hydroxyl radicals were ineffective.

Lastly, the stability of the BB-6 photocatalyst was evaluated by reuse studies to establish its practical applicability. After three reuse cycles, the activity of photocatalyst BB-6 in degrading TC reduced marginally, but the total degradation efficiency remained about 80%. According to the findings (Fig. 8(b)), the capacity to degrade TC with the light on remains excellent after three cycles, and the drop in total degradation ability is mostly attributable to a change in adsorption ability in the dark adsorption stage. When taken as a whole, its light degradation capability is generally steady. It has a lot of practical application potential.

3.4. Catalytic mechanism

The attack of photoliving chemicals (e.g., h^+ , $\cdot\text{OH}$, and $\cdot\text{O}_2^-$) on pollutants is central to the photodegradation process. As a result, the aforementioned free radical quenching experiments were used to further study the role of free radicals in TC degradation. The sequence of the reactive species involved in TC photodegradation is $\text{h}^+ > \cdot\text{O}_2^- > \cdot\text{OH}$.

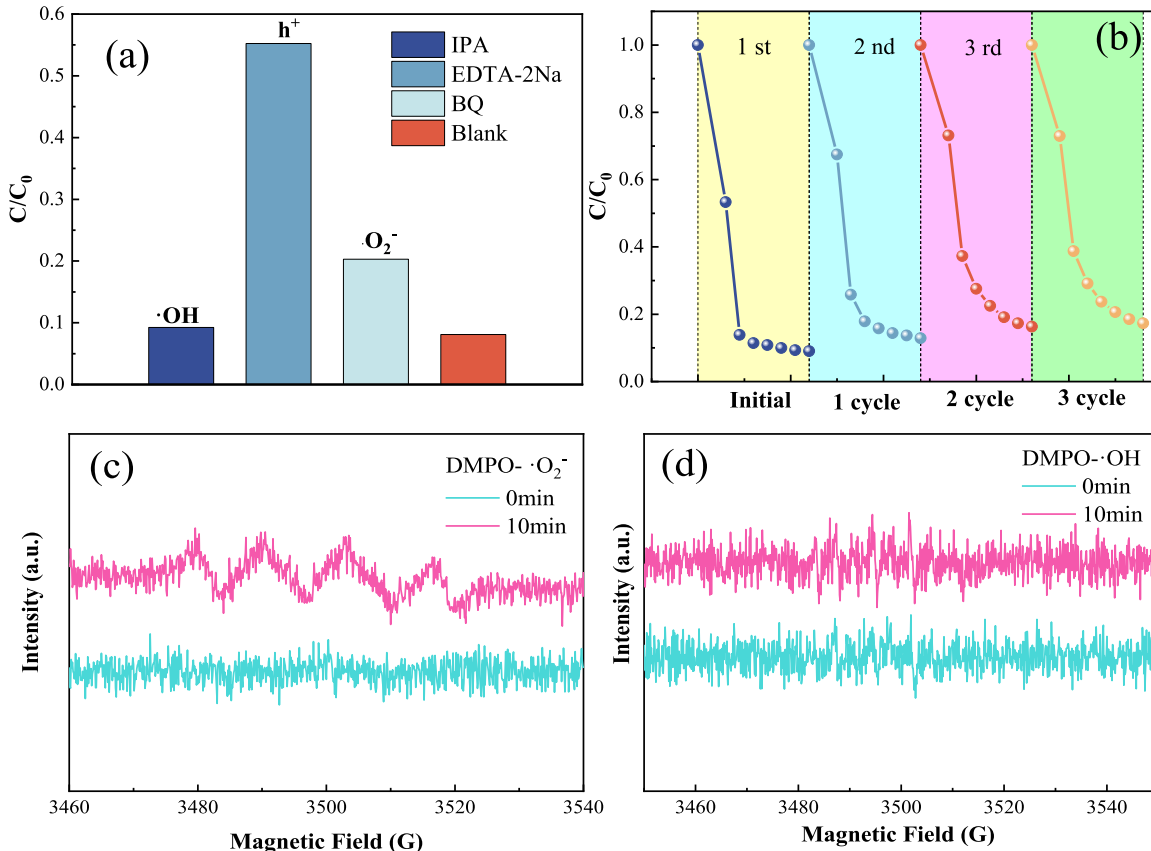


Fig. 8. (a) TC removal efficiency by BB-6 heterojunction with various scavengers under solar-light irradiation. (b) Reusing experiments of TC photodegradation over BB-6 heterojunction. (c)-(d) ESR electromagnetic spin resonance test results.

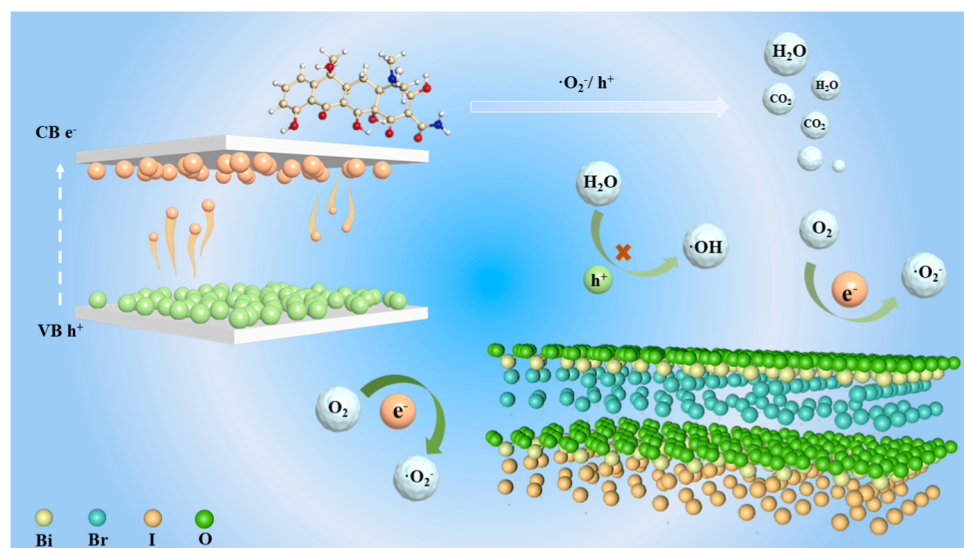
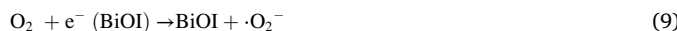


Fig. 9. The proposed mechanism of TC degradation in the BiOI/BiOBr photocatalytic system under solar light irradiation.

Fig. 9 proposes a probable charge separation and transfer mechanism of BiOI/BiOBr based on the contribution of the reactive species and the previously calculated energy band structure, and Eqs. ((7)–(11)) introduces the photocatalytic process.



As they come into touch, electrons flow from the high Fermi energy level side to the low Fermi energy level side until they reach equilibrium, and the side that loses electrons bends upward, while the side that obtains electrons bends downward. As a result of the electrons moving from BiOI to BiOBr to achieve the same Fermi level, VB and CB will bend owing to the Fermi level balancing [22,51,52]. Based on comparable reported materials and Fermi energy level locations, the traditional II heterojunction process may be the probable photocatalytic charge transfer mechanism in the TC photodegradation system on BB-6 (**Fig. 9**). When the oxidation and reduction potentials are compared, the CB values of BiOI and BiOBr are more negative than $(\text{O}_2/\cdot\text{O}_2^-) + 0.13$ eV vs. NHE, but the VB values are smaller than $(\text{OH}^-/\cdot\text{OH}) (2.68$ eV vs. NHE), which cannot oxidize water molecules to create hydroxyl radicals. Like a result, the vacancies on VB are still directly involved in the degradation reaction. This is consistent with the findings of the radical trapping tests. In summary, the general charge transfer process is that both BiOI and BiOBr photocatalysts may create e^- and h^+ , and the photogenerated e^- in BiOI's CB will migrate to BiOBr's CB due to the more negative position of BiOI's CB. Meanwhile, the holes in BiOBr's VB tend to diffuse to the more positive VB of BiOI. based on the radical burst studies, $\cdot\text{O}_2$ and h^+ are the principal reactive chemicals in the BB-6 catalytic system. The h^+ redox potential accumulated on the VB of BiOI, on the other hand, is too low to supply enough energy to produce hydroxyl radicals to participate in the process, but it can participate in the reaction directly as reactive chemicals. Overall, the electron transport mechanism of typical type II heterojunctions is preserved.

3.5. DFT calculation

3.5.1. Band structure and electron density difference

DFT simulations were used to analyze the energy band structure, density of states, and differential charge density of BiOI/BiOBr in order to investigate the electronic structural modification. The band gap values of BiOBr, BiOI, and BiOBr/BiOI are shown in **Fig. 10(a)–(c)**, respectively, and the theoretical value (2.185 eV/1.810 eV) is found to be close to the actual value (1.85 eV/1.67 eV) by calculation, and the band gap value (1.098 eV) is significantly reduced when the two are combined, demonstrating that the heterojunction. The charge transfer resistance of the composite is effectively lowered, and the light harvesting performance is improved with the help of the heterojunction. Later, the DOS of BiOI/BiOBr composites was calculated to further validate the heterostructural properties of the BiOI/BiOBr composites. **Fig. 10(e)** depicts the composites' total density of states (TDOS) and the partial density of states (PDOS) of BiOI and BiOBr in the composites, respectively. BiOBr/BiOI total density of states graphs are comparable to the computed. The PDOS of BiOI and BiOBr are very comparable and show a declining trend at the Fermi energy level, indicating that the two have a great matching relationship in the creation of heterojunctions. An in-depth observation of differential charge density is done to further expose the transfer rules of electrons at the constituted heterojunction interface, where yellow is the electron accumulation zone and green is the electron depletion region. According to **Fig. 10(d)**, electrons can be effectively transferred at the constituted heterojunction interface, and from the transfer direction, more from the BiOI interface to the BiOBr interface, confirming the experimentally proposed electron transfer mechanism of type II heterojunction.

The work functions of BiOI and BiOBr are 5.974 eV and 7.062 eV, respectively, as shown in **Fig. 10(f)–(g)**, and it can be seen from the figure that the Fermi energy level of BiOI is located at -9.72 eV and the Fermi energy level of BiOBr is located at -9.69 eV. Since the Fermi energy level of BiOI is obviously more negative than the position of The Fermi level balance causes VB and CB to be bent because the electrons tend to shift from BiOI to BiOBr so that the phases are at the same Fermi level. This allows electron enrichment from the BiOI surface to the BiOBr surface and boosts photogenerated electron transport. Thus, the photocatalytic charge transfer mechanism in the BiOI/BiOBr upper TC photodegradation system is a conventional II heterojunction mechanism, as demonstrated on the molecular scale by similarly reported materials and Fermi energy level positions. As a result of the photocatalytic activation of molecular oxygen, additional $\cdot\text{O}_2$ will be created.

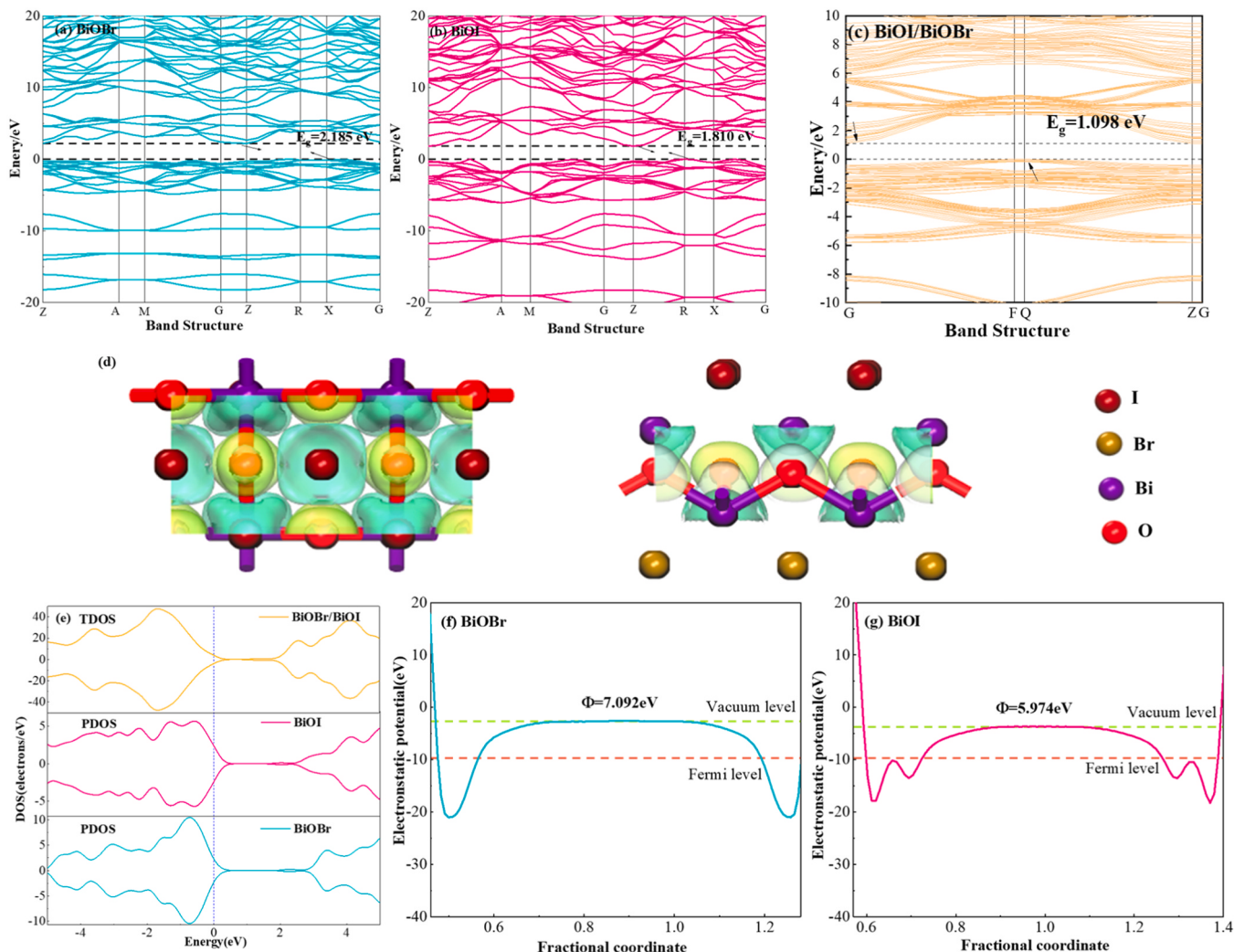


Fig. 10. (a)-(c) Bandgap values for BiOBr, BiOI, and BiOI/BiOBr. (b) Electron density difference diagram of BiOI(001)/BiOBr(001) surface. (e) Total and partial density of states BiOI(001)/BiOBr(001), BiOI(001) and BiOBr(001). (f)-(g)Work functions of BiOI (001) surface and BiOBr(001) surface.

In summary, density functional theory explains that when BiOI is compounded with BiOBr, a type-II heterojunction is formed reasonably, which is favorable for electron transfer and carrier separation, and more effective molecular oxygen activation and superoxide radicals are generated by adjusting the energy band position so that the bismuth halide oxide has a more negative conduction band position. This allows bismuth halide to maintain its conformation throughout a wide pH range while eliminating impurities in a more stable way.

Fig.S3 shows the calculated DFT models of the three catalysts (BiOI, BiOBr and BiOBr/BiOI) from different angles. The average bond lengths and adsorption energies of the three catalysts were determined after the activation of O_2 molecules. The average bond lengths and adsorption energies for BiOBr and BiOI in the pure phase are 1.237 Å, 1.238 Å and 0.0705 eV, 0.0235 eV, respectively, while the O_2 bond length and adsorption energy on the BiOBr/BiOI surface are much larger than those of the pure-phase BiOBr and BiOI, 1.242 Å and 0.0860 eV, respectively, indicating that the adsorption of O_2 can be increased when both form a heterojunction structure, which promotes the activation of O_2 and the generation of more superoxide radicals.

3.5.2. Frontier orbitals

The various morphologies of tetracycline at different pH levels were initially examined to understand the influence of pH on tetracycline. Tetracycline has a benzene ring, a ketone group, and an enol group in its

structure. When TC-HCl is mixed with water, protonated TC (TC^1) is produced [53]. As well as the shape of TC varies as the pH changes. When the pH rises, TC begins to deprotonate. Tetracycline's major deprotonation site is at positions 1–4. Site 1 is deprotonated when the pH falls below 3.99 (TC^0). Sites 1 and 2 are deprotonated in the pH range of 3.99–6.34 (TC^{-1}). Deprotonation occurs at sites 1, 2, and 3 in the pH range of 6.34–10.36 (TC^{-2}). Ultimately, in the pH range of 10.36–12.03, all four sites were deprotonated (TC^{-3}) [54].

The HOMO orbitals of TC^1 and TC^{-1} (Fig. 11(a), 11(c)) are mostly centered on the fourth six-membered ring, $[-N(CH_3)_2]$ and the surrounding oxygen-containing functional groups, as shown in Fig. 11. The HOMO orbitals of TC^0 and TC^{-2} (Figs. 11(b) and 11(d)), on the other hand, are all substantially centered on the oxygen-containing functional group near the fourth six-membered ring. On the other hand (Fig. 11(e)), is largely concentrated in the first three six-membered rings. Because the molecule's HOMO is less tightly bonded to its electrons and has the character of an electron donor, the higher the HOMO, the stronger the electron donating capacity and the easier it is to oxidize [55]. As a result, when the TC is in the form of TC^0 , TC^{-1} , or TC^{-2} , the fourth six-membered ring and the oxygen-containing functional group, $[-N(CH_3)_2]$, as well as other sites in its vicinity, are more likely to lose electrons to oxidation, whereas when the TC is in the form of TC^{-3} , which is strongly basic, the benzene ring is more likely to lose electrons. According to bond energy, the benzene ring needs significantly more

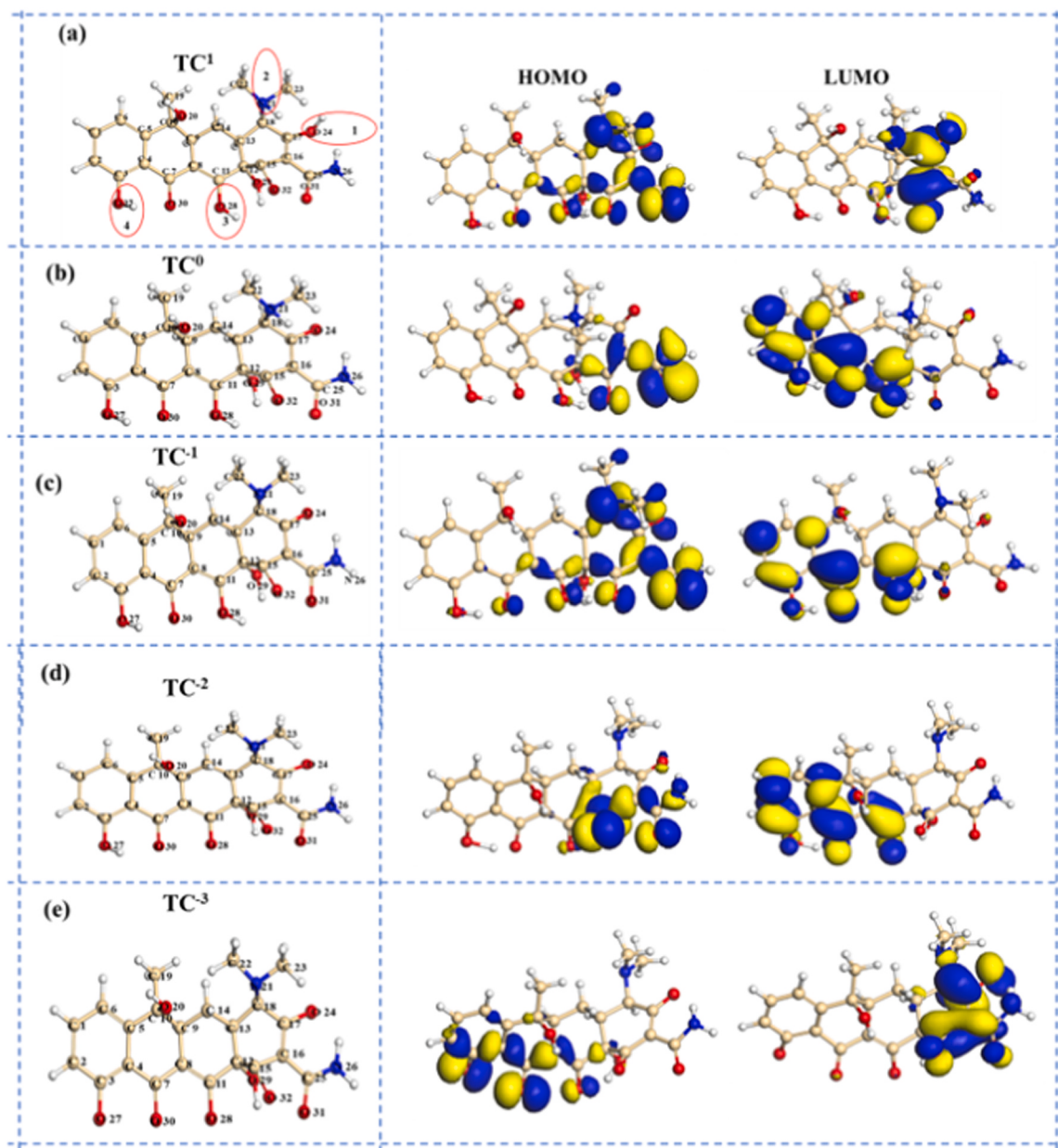


Fig. 11. HOMO and LUMO orbitals corresponding to TCs in different deprotonation forms.

energy to break than other functional groups, hence the TC^{-3} form in the strong base state is more difficult to remove than the other forms of TC. The main concentration of HOMO orbitals for TC^0 , TC^{-1} , and TC^{-2} is on [-CO(NH₂)], with HOMO values of -0.176314, -0.078478, and +0.054015 Ha, respectively (see Table 1 for the relevant data). The HOMO values show that the greater the negative potential as the pH of the solution lowers, the greater the propensity to be oxidized. As a result, when the pH lowers, the capacity to donate electrons on the fourth six-membered ring and the surrounding oxygen-containing functional

groups increases, and because the above places have two C-N structures on the tetracycline, the C-N bond is more active than the benzene ring structure. Tetracycline would thus be more prone to bond breaking cleavage, making it more susceptible to deterioration. This conclusion is consistent with the outcomes of the experiments.

3.5.3. Fukui function and electrostatic potential analysis

The Fukui function of tetracycline and electrostatic potential analyses were then used to generate a tentative forecast of the reaction site in order to derive the degradation route [1,56].

Fig. 12 depicts the distribution of electrostatic potentials on the surface of TC molecules at various pH levels, with blue representing negative potentials and red representing positive potentials. More blue patches form in the lower half of the image as deprotonation deepens (Fig. 12(a)), possibly because to the substantial negative contribution of the lone pair of electrons to the electrostatic potential. TC^0 (Fig. 12(b)) has more negative potential areas and is more concentrated around oxygen-containing functional groups. This makes electrophilic reagents

Table 1
HOMOs and LUMOs of matrix.

Item	HOMO (Ha)	LUMO (Ha)
TC^1	-0.300069	-0.246733
TC^0	-0.176314	-0.111792
TC^{-1}	-0.078478	+ 0.002548
TC^{-2}	+ 0.054015	+ 0.120034
TC^{-3}	+ 0.185669	+ 0.25713

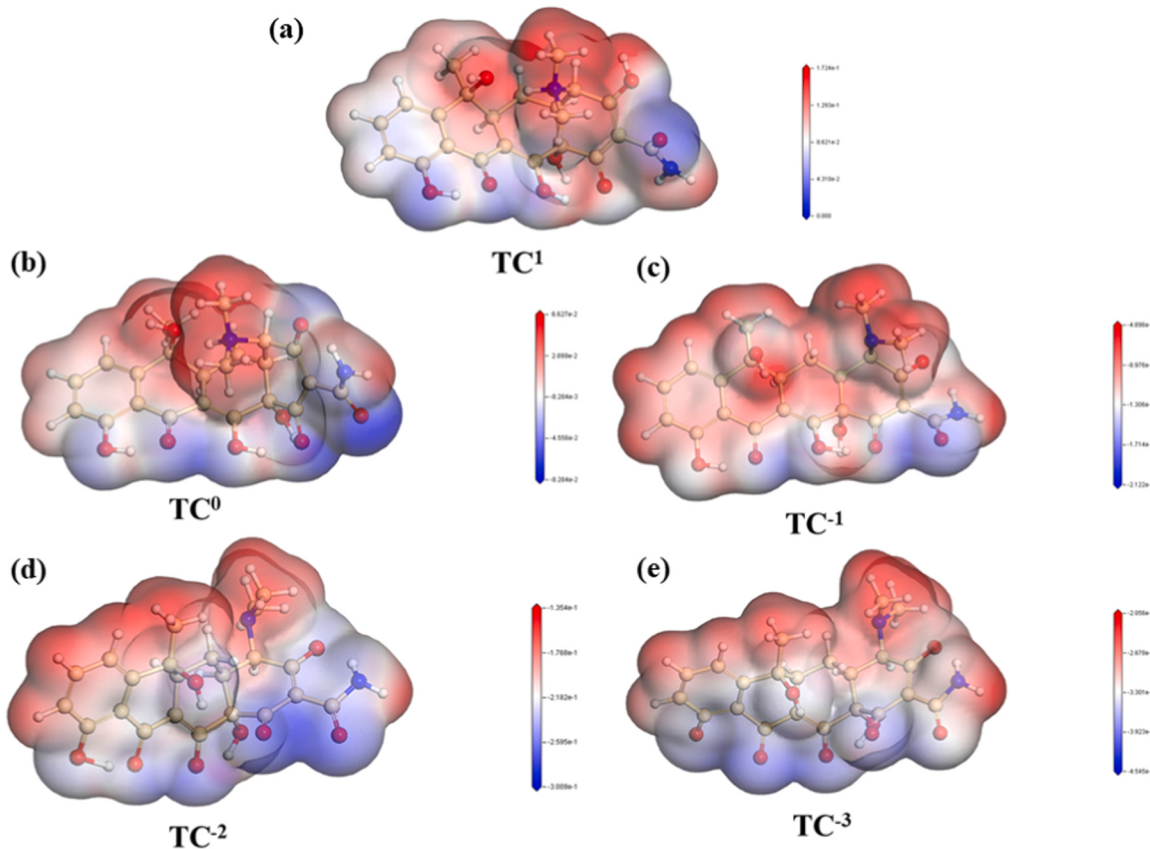


Fig. 12. ESP mapping of TC in different forms.

more susceptible to assault, allowing h^+ to target more sites and hasten TC cleavage.

The Fukui function was then used to assess the TC molecules in different states in order to forecast the likely reaction sites more intuitively and clearly. When TC is protonated, the particular sites of electrophilic radical attack are mostly concentrated on C6 and O27, whereas the specific sites of nucleophilic radical attack are concentrated on C15, C17, O24, and O32. When the pH progressively decreases and deprotonation occurs, the primary sites of electrophilic and nucleophilic radical assault begin to alter. In the TC^0 form, the f values of N26 and O31 on the [-CONH₂] functional group are 0.086 and 0.259, respectively, while the higher f^+ values emerge on C7 and O30 with 0.073 and 0.077, which are much higher than the other locations. As a result, in the TC^0 state, electrophilic radicals are more likely to target N26 and O31, whereas nucleophilic radicals are more likely to attack C7 and O30. Only the O31 f value stands out in the TC^{-1} state, reaching 0.127, while the O30 f^+ value shines out little, reaching 0.075. When the pH rises to TC^{-2} , the O31 and O32 sites become more sensitive to electrophilic radicals, with f values reaching 0.095 and 0.166, respectively, while C1 becomes the most vulnerable, with a f^+ value of 0.073. C1, with a f^+ value of 0.073, becomes the site most sensitive to nucleophilic radical assault. When the pH of the solution reaches a high base level, the spots most sensitive to electrophilic radical assault are O27 and O30, where f values can reach 0.136, and C17, O24, and O32, where f^+ values are 0.093, 0.081, and 0.075, respectively (Tables S1-S5). Consider the integrated free radical attack site f^0 [57]. When the pH changes, the main radical attack sites for TC^0 are O31 and N26, for TC^{-1} O31, O30, for TC^{-2} O32, O31, and for TC^{-3} O27 and O30, and the main bond-breaking sites involved can be summarized as amide groups as well as oxygen-containing functional groups around tetracyclines. As the pH rises, free radicals prefer to target the oxygen-containing functional group locations, and from the standpoint of bond energy, the bond

breaking of C=O demands more energy and is more difficult. Since a rise in pH enables free radicals to target the tough to break C=O, it makes tetracycline breakdown more difficult.

3.6. The degradation process of TC and its toxicity evolution

The DFT calculations for tetracycline itself were performed in Section 3.5, and because exceptionally strong acidic and alkaline environments are uncommon in normal life, appropriate degradation routes based on natural experimental circumstances were chosen for investigating tetracycline breakdown. Nevertheless, due to the effect of reaction rate, unstable or unknown intermediates, three important pathways were loosely established by integrating mechanistic analysis (Fig. 13), active substance burst data, DFT calculations, intermediates, and current study results. Moreover, the hypothesized degradation intermediates and routes were integrated to differentiate the various reaction sites by assessing the relative electrostatic potentials, therefore identifying the function of free radicals in the cleavage process (Fig. S2). The relevant cleavage fragments by LC-MS are shown in Fig. S4.

In pathway I, first TC attacks the amide group via the electrophilic radical h^+ to form A1 ($m/z = 362$), then $\cdot\text{O}_2$ attacks the O24 site, followed by ring-opening cleavage to form A2 ($m/z = 351$), at which point h^+ and $\cdot\text{O}_2$ attack the hydroxyl radical later formed at the C12 site with the methyl group on C10 to form A3 ($m/z = 274$) [53,58]. In pathway II, B1 ($m/z = 432$) is often the result of TC degradation by nucleophilic radical elimination of methyl groups on tertiary amines [59]. Electrophilic radicals attack the amide group and the active C-N bond to create B2 ($m/z = 407$) and B3 ($m/z = 396$), followed by continued ring cleavage to form B4 ($m/z = 300$) and B5 ($m/z = 130$) [53]. In pathway III, the hydroxyl group at the O24 site corresponding to TC is attacked by superoxide radicals and holes to generate D1 ($m/z = 388$), which is then dehydrated condensation to form D2 ($m/z = 340$) [53], followed by ring

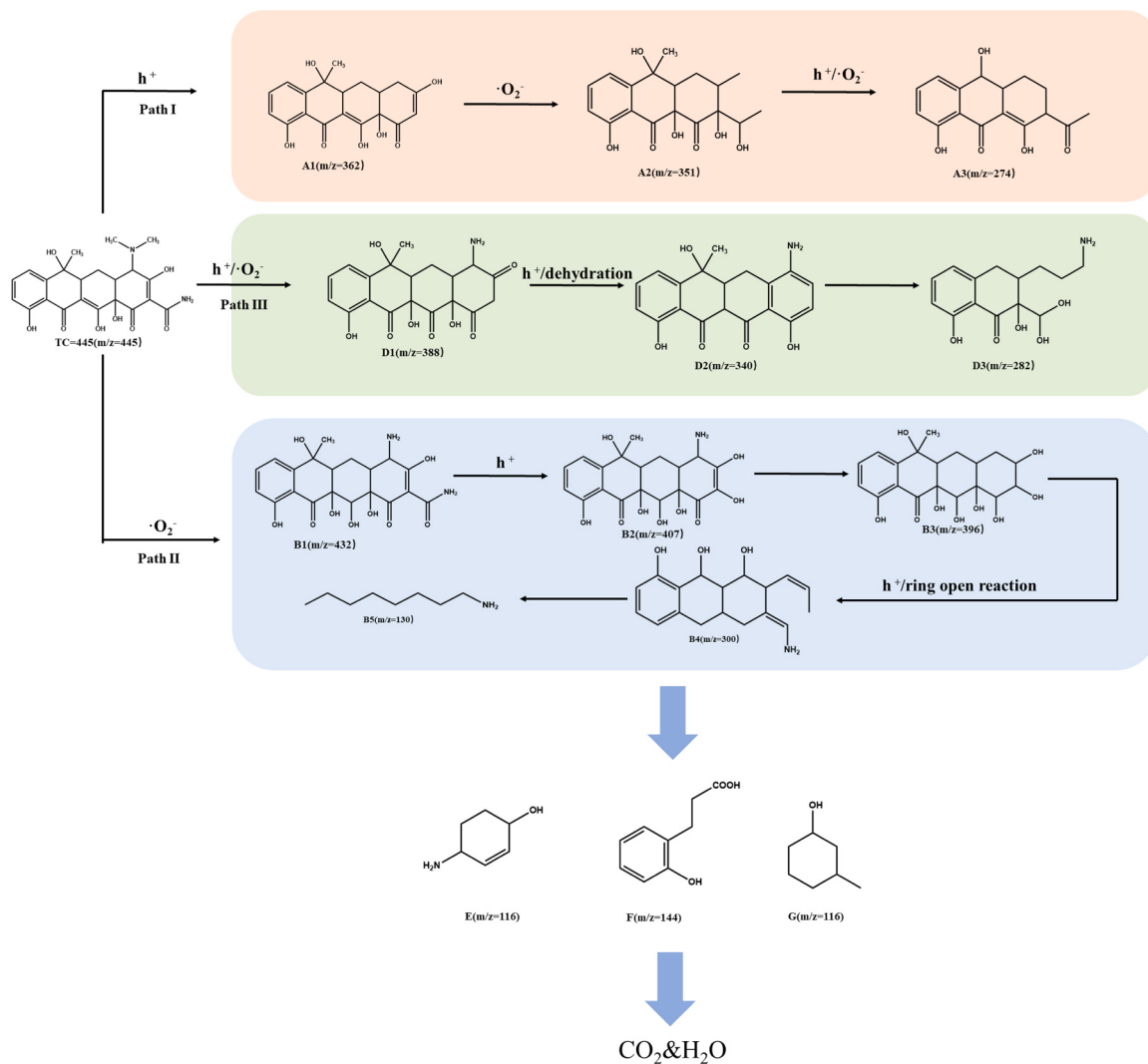


Fig. 13. The proposed degradation pathways for TC.

opening to form D3 ($m/z = 282$) [59]. It is worth noting that these TC degradation processes are not fully separate, and because organic reactions are complicated, these intermediates are likely to convert into one other even in distinct pathways [53].

Several of the intermediates generated during the reaction may be more hazardous during the photocatalytic process. QSAR prediction-based mathematical models [1]. T.E.S.T. software was used to evaluate four index factors: acute toxicity, bioconcentration, developmental toxicity, and mutagenicity. As shown in Fig. 14(a), the LC₅₀ (96 h) values of blackhead minnow were generally greater than the TC (0.9 mg/L) values for all intermediates, and an increase in LC₅₀ was observed for almost all degradation intermediates (except intermediate D2), indicating a significant decrease in the acute toxicity of the intermediates. Fig. 14(b) shows that the bioaccumulation factor of TC increased during the photolysis process, but because the intermediates discussed were all intermediates with intact structures, the increase in bioaccumulation factor could be avoided by extending the photocatalytic reaction time to thoroughly fragment the intermediates.

Fig. 14(c)-(d), on the other hand, show that when compared to TC, the developmental toxicity and mutagenicity of the intermediates are significantly reduced during photodegradation. For example, the developmental toxicity of all the degradation intermediates can be seen to be reduced compared to TC, except for Intermediate A3, which is slightly more developmentally toxic than TC, and Intermediate G, which is even predicted to be "developmentally non-toxic". Fig. 14(d)

demonstrates that the mutagenicity of several intermediates is elevated compared to TC and even some intermediates are categorized as "mutagenic positive". Nonetheless, the mutagenicity of many intermediates, particularly as the photocatalytic process progresses, is lower than that of the parent tetracycline and is decreasing. Some of the toxicity of the TC breakdown intermediates was reduced based on the projected environmental toxicity. Some of the breakdown intermediates, however, became more hazardous. Additionally, the degradation studies revealed that after 90 min of UV irradiation, TC was almost completely destroyed by BB-6, while some intermediates remained visible in LC-MS analysis. As a result, extending the degradation period is required to obtain high mineralization and therefore assure the eradication of toxicity of pollutants during photocatalytic degradation.

4. Conclusion

In sum up, in terms of materials, hydrothermal methods were used to successfully construct BiOI/BiOBr photocatalysts. Photodegradation of TC under solar irradiation was used to test the photocatalytic activity of the prepared photocatalysts. BB-6 demonstrated the highest photocatalytic activity and could completely remove TC in 90 min, and this catalyst has a wide pH adaptability, maintaining 80% degradation efficiency in the pH range of 3–11. Additionally, cyclic experiments have shown that BB-6 has a high potential for practical applications.

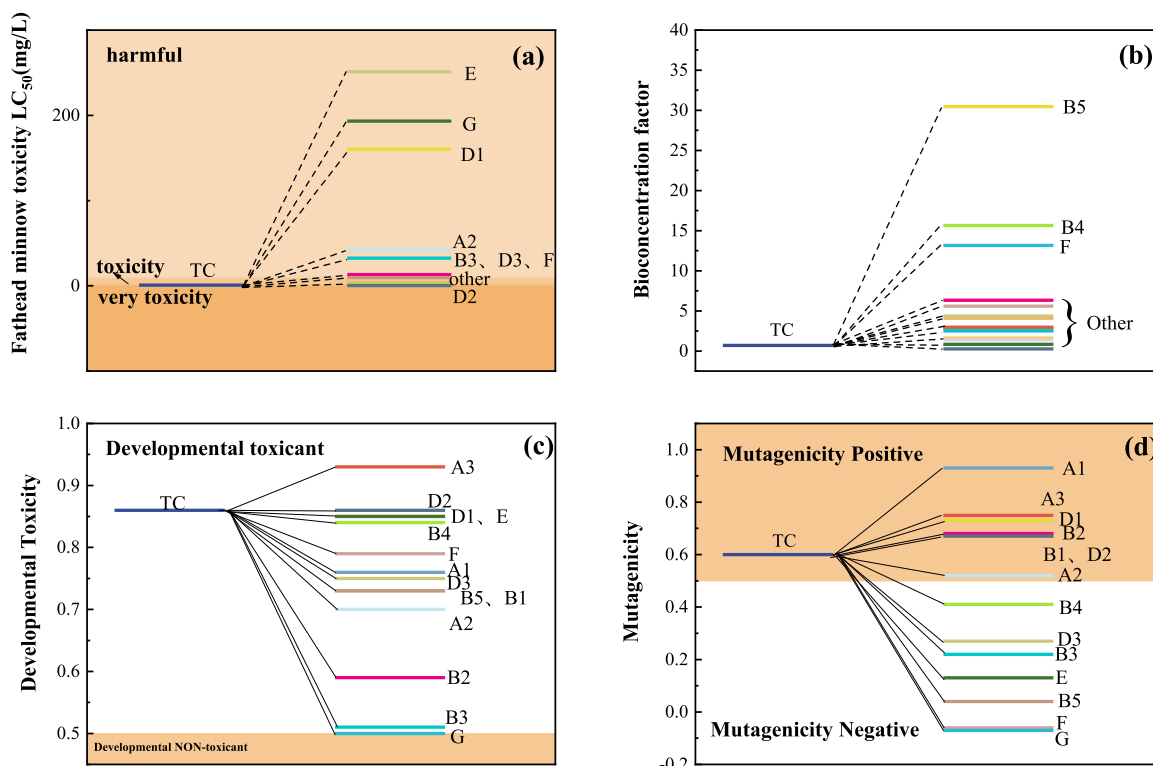


Fig. 14. (a) Acute toxicity, (b) bioaccumulation factor, (c) developmental toxicity, and (d) mutagenicity of TC and degradation intermediates.

Furthermore, by combining density functional theory (DFT) calculations at the molecular scale, we discovered a correlation between the properties of tetracycline and the photocatalytic degradation mechanism at different pH values, as well as gained insight into the charge transfer mechanism at the heterojunction interface. Coupled with LC-MS to investigate the relevant tetracycline intermediates in generalized circumstances and forecast the reaction route. The toxicity of intermediates formed in the probable photocatalytic breakdown route of TC was also determined using QSAR predictions. This study offers fresh insights into the breakdown of antibiotics under various pH environments.

CRediT authorship contribution statement

Qianqian Ni: Data curation, Writing – original draft preparation, Methodology; **Xin Ke:** Visualization, Investigation, Writing – review & editing. **Wenjing Qian:** Conceptualization, Software; **Zheng Yan** and **JingDe Luan:** Supervision. **Wengang Liu:** Software, Supervision. All authors have read and agreed to the published version of the manuscript.

Declaration of Competing Interest

The authors declare that they have no known competing financial interests or personal relationships that could have appeared to influence the work reported in this paper.

Data Availability

Data will be made available on request.

Acknowledgments

This research was supported by Liaoning Revitalization Talents Program [XLYC1807045], and Shenyang Young and Middle-aged Science and Technology Innovation Talent Support Program [RC180101].

We thank the Key Laboratory of Clean Energy, Liaoning Province and Shenyang Aerospace University College of Energy and Environment for their scientific research assistance.

Appendix A. Supporting information

Supplementary data associated with this article can be found in the online version at doi:10.1016/j.apcatb.2023.123226.

References

- [1] Z.X. Liu, Y.D. Liu, X.B. Sun, H.D. Ji, W. Liu, Z.Q. Cai, Construction of Z-scheme Ag/AgVO₃/carbon-rich g-C₃N₄ heterojunction for enhanced photocatalytic degradation of sulfamethidiazole: DFT calculation and mechanism study, Chem. Eng. J. 433 (2022), 133604.
- [2] X. Chu, G. Shan, C. Chang, Y. Fu, L. Yue, L. Zhu, Effective degradation of tetracycline by mesoporous Bi₂WO₆ under visible light irradiation, Front. Environ. Sci. Eng. 10 (2014) 211–218.
- [3] D. Jiang, T. Wang, Q. Xu, D. Li, S. Meng, M. Chen, Perovskite oxide ultrathin nanosheets/g-C₃N₄ 2D–2D heterojunction photocatalysts with significantly enhanced photocatalytic activity towards the photodegradation of tetracycline, Appl. Catal. B: Environ. 201 (2017) 617–628.
- [4] X. Zhang, J. Chen, S. Jiang, X. Zhang, F. Bi, Y. Yang, Y. Wang, Z. Wang, Enhanced photocatalytic degradation of gaseous toluene and liquidus tetracycline by anatase/rutile titanium dioxide with heterophase junction derived from materials of Institut Lavoisier-125(Ti): Degradation pathway and mechanism studies, J. Colloid Interface Sci. 588 (2021) 122–137.
- [5] X. Wei, H. Feng, L. Li, J. Gong, K. Jiang, S. Xue, P.K. Chu, Synthesis of tetragonal prismatic γ-In₂Se₃ nanostructures with predominantly {110} facets and photocatalytic degradation of tetracycline, Appl. Catal. B: Environ. 260 (2020), 118218.
- [6] E.R. Mojica, E. Nguyen, M. Rozov, F.V. Bright, pH-dependent spectroscopy of tetracycline and its analogs, J. Fluor. 24 (2014) 1183–1198.
- [7] Y. Meng, X. Chen, D. Ai, T. Wei, Z. Fan, B. Wang, Sulfur-doped zero-valent iron supported on biochar for tetracycline adsorption and removal, J. Clean. Prod. 379 (2022), 134769.
- [8] P. Bhatt, C.H. Jeon, W. Kim, Tetracycline bioremediation using the novel *Serratia marcescens* strain WW1 isolated from a wastewater treatment plant, Chemosphere 298 (2022), 134344.
- [9] X. Wang, H. Zhang, W. Wang, G. Zhang, X. Chu, J. Cao, Synthesis of 1D/2D Bi₂S₃@TiC₂ heterojunction with superior photocatalytic removal ability of tetracycline hydrochloride, Mater. Lett. 326 (2022), 132907.

[10] F. Yan, Y. Wang, C. Yi, J. Xu, B. Wang, R. Ma, M. Xu, Construction of carbon dots modified Cl-doped Bi₂WO₆ hollow microspheres for boosting photocatalytic degradation of tetracycline under visible light irradiation, *Ceram. Int.* 49 (2023) 7214–7222.

[11] M. Chen, J. Yao, Y. Huang, H. Gong, W. Chu, Enhanced photocatalytic degradation of ciprofloxacin over Bi₂O₃/(BiO)₂CO₃ heterojunctions: Efficiency, kinetics, pathways, mechanisms and toxicity evaluation, *Chem. Eng. J.* 334 (2018) 453–461.

[12] M. Chen, W. Chu, J. Beiyuan, Y. Huang, Enhancement of UV-assisted TiO₂ degradation of ibuprofen using Fenton hybrid process at circumneutral pH, *Chin. J. Catal.* 39 (2018) 701–709.

[13] M. Chen, Y. Huang, W. Chu, Exploring a broadened operating pH range for norfloxacin removal via simulated solar-light-mediated Bi₂WO₆ process, *Chin. J. Catal.* 40 (2019) 673–680.

[14] E.S. Elmolla, M. Chaudhuri, Degradation of amoxicillin, ampicillin and cloxacillin antibiotics in aqueous solution by the UV/ZnO photocatalytic process, *J. Hazard Mater.* 173 (2010) 445–449.

[15] W. Chu, W.K. Choy, T.Y. So, The effect of solution pH and peroxide in the TiO₂-induced photocatalysis of chlorinated aniline, *J. Hazard Mater.* 141 (2007) 86–91.

[16] A. Hussain, J.H. Hou, M. Tahir, S.S. Ali, Z.U. Rehman, M. Bilal, T.T. Zhang, Q. Dou, X.Z. Wang, Recent advances in BiOX-based photocatalysts to enhanced efficiency for energy and environment applications, *Catal. Rev. -Sci. Eng.* (2022) 55.

[17] S. Singh, R. Sharma, M. Khanuja, A review and recent developments on strategies to improve the photocatalytic elimination of organic dye pollutants by BiOX (X=Cl, Br, I, F) nanostructures, *Korean J. Chem. Eng.* 35 (2018) 1955–1968.

[18] Y. Shi, H. Li, C. Mao, G. Zhan, Z. Yang, C. Ling, K. Wei, X. Liu, Z. Ai, L. Zhang, Manipulating excitonic effects in layered bismuth oxyhalides for photocatalysis, *ACS EST Eng.* 2 (2022) 957–974.

[19] Y. Jiang, H.Y. Chen, J.Y. Li, J.F. Liao, H.H. Zhang, X.D. Wang, D.B. Kuang, Z-Scheme 2D/2D heterojunction of CsPbBr₃/Bi₂WO₆ for improved photocatalytic CO₂ reduction, *Adv. Funct. Mater.* 30 (2020) 2004293.

[20] H. Shi, C. Li, L. Wang, W. Wang, X. Meng, Selective reduction of nitrate into N₂ by novel Z-scheme NH₂-MIL-101(Fe)/BiVO₄ heterojunction with enhanced photocatalytic activity, *J. Hazard Mater.* 424 (2022), 127711.

[21] H. Ben, Y. Liu, X. Liu, X. Liu, C. Ling, C. Liang, L. Zhang, Diffusion-controlled Z-scheme-steered charge separation across PDI/BiOI heterointerface for ultraviolet, visible, and infrared light-driven photocatalysis, *Adv. Funct. Mater.* 31 (2021) 2102315.

[22] C. Liu, S. Mao, M. Shi, X. Hong, D. Wang, F. Wang, M. Xia, Q. Chen, Enhanced photocatalytic degradation performance of BiVO₄/BiOBr through combining Fermi level alteration and oxygen defect engineering, *Chem. Eng. J.* 449 (2022), 137757.

[23] J. Chen, H. Liu, L. Zhu, Z. Fu, Y. Lu, One-pot synthesis of Bi₂TiO₄F₂/BiOBr ferroelectric heterostructure for photocatalytic oxygen evolution, *J. Alloy. Compd.* 873 (2021), 159847.

[24] X. Li, B. Han, X. Wang, P. Bai, L. Sun, Q. Hao, K. Yu, C. Liang, High photocatalytic activity of rutile TiO₂-BiOBr composites via an in situ synthesis approach, *N. J. Chem.* 44 (2020) 1905–1911.

[25] C. Song, P. Chen, C. Wang, L. Zhu, Photodegradation of perfluorooctanoic acid by synthesized TiO₂-MWCNT composites under 365nm UV irradiation, *Chemosphere* 86 (2012) 853–859.

[26] F. Li, Z. Wei, K. He, L. Blaney, X. Cheng, T. Xu, W. Liu, D. Zhao, A concentrate-and-destroy technique for degradation of perfluorooctanoic acid in water using a new adsorptive photocatalyst, *Water Res* 185 (2020), 116219.

[27] Y. Zhu, H. Ji, K. He, L. Blaney, T. Xu, D. Zhao, Photocatalytic degradation of GenX in water using a new adsorptive photocatalyst, *Water Res* 220 (2022), 118650.

[28] X. Peng, C. Liu, Z. Zhao, F. Hu, H. Dai, Construction of a Z-scheme g-C₃N₄/NBGO/BiVO₄ heterostructure with visible-light driven photocatalytic degradation of tetracycline: efficiency, reaction pathway and mechanism, *Catal. Sci. Technol.* 12 (2022) 1339–1358.

[29] K. Gao, L.-a Hou, X. An, D. Huang, Y. Yang, BiOBr/MXene/gC₃N₄ Z-scheme heterostructure photocatalysts mediated by oxygen vacancies and MXene quantum dots for tetracycline degradation: Process, mechanism and toxicity analysis, *Appl. Catal. B: Environ.* 323 (2023) 122150.

[30] Y. Dong, X. Wang, H. Sun, H. Zhang, X. Zhao, L. Wang, Construction of a 0D/3D AgI/MOF-808 photocatalyst with a one-photon excitation pathway for enhancing the degradation of tetracycline hydrochloride: Mechanism, degradation pathway and DFT calculations, *Chem. Eng. J.* 460 (2023), 141842.

[31] Z. Shi, Y. Zhang, X. Shen, G. Duoerkun, B. Zhu, L. Zhang, M. Li, Z. Chen, Fabrication of g-C₃N₄/BiOBr heterojunctions on carbon fibers as weaveable photocatalyst for degrading tetracycline hydrochloride under visible light, *Chem. Eng. J.* 386 (2020), 124010.

[32] W. Zhang, Z. Bian, Y. Peng, H. Tang, H. Wang, Dual-function oxygen vacancy of BiOBr intensifies pollutant adsorption and molecular oxygen activation to remove tetracycline hydrochloride, *Chem. Eng. J.* 451 (2023), 138731.

[33] D. Dolat, N. Quici, E. Kusiak-Nejman, A.W. Morawski, G. Li, Puma, one-step, hydrothermal synthesis of nitrogen, carbon co-doped titanium dioxide (N, CTiO₂) photocatalysts. Effect of alcohol degree and chain length as carbon dopant precursors on photocatalytic activity and catalyst deactivation, *Appl. Catal. B: Environ.* 115–116 (2012) 81–89.

[34] A. Gora, B. Toepfer, V. Puddu, G. Li Puma, Photocatalytic oxidation of herbicides in single-component and multicomponent systems: Reaction kinetics analysis, *Appl. Catal. B: Environ.* 65 (2006) 1–10.

[35] P. Soriano-Molina, J.L. García Sánchez, S. Malato, L.A. Pérez-Estrada, J.A. Sánchez Pérez, Effect of volumetric rate of photon absorption on the kinetics of micropollutant removal by solar photo-Fenton with Fe3+-EDDS at neutral pH, *Chem. Eng. J.* 331 (2018) 84–92.

[36] J. Korać Jačić, M.R. Milenković, D. Bajuk-Bogdanović, D. Stanković, M. Dimitrijević, I. Spasojević, The impact of ferric iron and pH on photo-degradation of tetracycline in water, *J. Photochem. Photobiol. A: Chem.* 433 (2022), 114155.

[37] R. Bibi, Q. Shen, L. Wei, D. Hao, N. Li, J. Zhou, Hybrid BiOBr/UiO-66-NH₂ composite with enhanced visible-light driven photocatalytic activity toward RhB dye degradation, *RSC Adv.* 8 (2018) 2048–2058.

[38] J. Di, J. Xia, M. Ji, B. Wang, S. Yin, Q. Zhang, Z. Chen, H. Li, Advanced photocatalytic performance of graphene-like BN modified BiOBr flower-like materials for the removal of pollutants and mechanism insight, *Appl. Catal. B: Environ.* 183 (2016) 254–262.

[39] J. Han, G. Zhu, M. Hojaberdiiev, J. Peng, X. Zhang, Y. Liu, B. Ge, P. Liu, Rapid adsorption and photocatalytic activity for Rhodamine B and Cr(vi) by ultrathin BiOI nanosheets with highly exposed {001} facets, *N. J. Chem.* 39 (2015) 1874–1882.

[40] Z. Wei, X. Dong, N. Zheng, Y. Wang, X. Zhang, H. Ma, Novel visible-light irradiation niobium-doped BiOBr microspheres with enhanced photocatalytic performance, *J. Mater. Sci.* 55 (2020) 16522–16532.

[41] X. Yang, Z. Chen, W. Zhao, C. Liu, X. Qian, W. Chang, T. Sun, C. Shen, G. Wei, Construction of porous-hydrangea BiOBr/BiOI n-n heterojunction with enhanced photodegradation of tetracycline hydrochloride under visible light, *J. Alloy. Compd.* 864 (2021), 158784.

[42] R. Ning, H. Pang, Z. Yan, Z. Lu, Q. Wang, Z. Wu, W. Dai, L. Liu, Z. Li, G. Fan, X. Fu, An innovative S-scheme AgCl/MIL-100(Fe) heterojunction for visible-light-driven degradation of sulfamethazine and mechanism insight, *J. Hazard Mater.* 435 (2022), 129061.

[43] X. Liu, Z. Yang, L. Zhang, In-situ fabrication of 3D hierarchical flower-like beta-Bi₂O₃/CoO Z-scheme heterojunction for visible-driven simultaneous degradation of multi-pollutants, *J. Hazard Mater.* 403 (2021), 123566.

[44] Q. Ni, S. Feng, X. Ke, Z. Yan, J. Luan, Multi-dimensional (2D–3D) assembly of BiOI/BiOBr/UiO-66-NH₂ composites to form multi-heterojunction structures for synergistic removal of Rhodamine B, *J. Alloy. Compd.* 935 (2023), 168103.

[45] R. Saravanan, E. Sacari, F. Gracia, M.M. Khan, E. Mosquera, V.K. Gupta, Conducting PANI stimulated ZnO system for visible light photocatalytic degradation of coloured dyes, *J. Mol. Liq.* 221 (2016) 1029–1033.

[46] T. Jia, J. Wu, Z. Ji, C. Peng, Q. Liu, M. Shi, J. Zhu, H. Wang, D. Liu, M. Zhou, Surface defect engineering of Fe-doped Bi₇O₉I₃ microflowers for ameliorating charge-carrier separation and molecular oxygen activation, *Appl. Catal. B: Environ.* 284 (2021), 119727.

[47] R. Bariki, D. Majhi, K. Das, A. Behera, B.G. Mishra, Facile synthesis and photocatalytic efficacy of UiO-66/CdIn₂S₄ nanocomposites with flowerlike 3D-microspheres towards aqueous phase decontamination of triclosan and H₂ evolution, *Appl. Catal. B: Environ.* 270 (2020), 118882.

[48] R. Bariki, S.K. Pradhan, S. Panda, S.K. Nayak, A.R. Pati, B.G. Mishra, Hierarchical UiO-66-(NH₂)/CuInS₂(S)-Scheme Photocatalyst with Controlled Topology for Enhanced Photocatalytic N(2) Fixation and H₂O₂ Production, *Langmuir* 39 (2023) 7707–7722.

[49] Z. Xie, Y. Feng, F. Wang, D. Chen, Q. Zhang, Y. Zeng, W. Lv, G. Liu, Construction of carbon dots modified MoO₃/g-C₃N₄ Z-scheme photocatalyst with enhanced visible-light photocatalytic activity for the degradation of tetracycline, *Appl. Catal. B: Environ.* 229 (2018) 96–104.

[50] J. Xiong, X. Li, J. Huang, X. Gao, Z. Chen, J. Liu, H. Li, B. Kang, W. Yao, Y. Zhu, CN/rGO@BPQDs high-low junctions with stretching spatial charge separation ability for photocatalytic degradation and H₂O₂ production, *Appl. Catal. B: Environ.* 266 (2020), 118602.

[51] F. Xu, K. Meng, B. Cheng, S. Wang, J. Xu, J. Yu, Unique S-scheme heterojunctions in self-assembled TiO₂/CsPbBr₃ hybrids for CO₂ photoreduction, *Nat. Commun.* 11 (2020) s41467-020-18350-7.

[52] X. Xiong, J. Zhang, C. Chen, S. Yang, J. Lin, J. Xi, Z. Kong, Novel 0D/2D Bi₂WO₆/MoSSe Z-scheme heterojunction for enhanced photocatalytic degradation and photoelectrochemical activity, *Ceram. Int.* 48 (2022) 31970–31983.

[53] R. Tang, D. Gong, Y. Deng, S. Xiong, J. Zheng, L. Li, Z. Zhou, L. Su, J. Zhao, pi-pi stacking derived from graphene-like biochar/g-C₃N₄ with tunable band structure for photocatalytic antibiotics degradation via peroxyomonosulfate activation, *J. Hazard Mater.* 423 (2022), 126944.

[54] W. Zuo, N. Li, B. Chen, C. Zhang, Q. Li, M. Yan, Investigation of the deprotonation of tetracycline using differential absorbance spectra: a comparative experimental and DFT/TD-DFT study, *Sci. Total Environ.* 726 (2020), 138432.

[55] H. Ji, P. Du, D. Zhao, S. Li, F. Sun, E.C. Duin, W. Liu, 2D/1D graphic carbon nitride/titanate nanotubes heterostructure for efficient photocatalysis of sulfamethazine under solar light: catalytic “hot spots” at the rutile-anatase-titanate interfaces, *Appl. Catal. B: Environ.* 263 (2020), 118357.

[56] A. Mahmood, S.I. Jones, P. Tao, B.G. Janesko, An orbital-overlap complement to ligand and binding site electrostatic potential maps, *J. Chem. Inf. Model* 58 (2018) 1836–1846.

[57] F. Liu, J. Liang, L. Chen, M. Tong, W. Liu, Photocatalytic removal of diclofenac by Ti doped BiOI microspheres under visible light irradiation: Kinetics, mechanism, and pathways, *J. Mol. Liq.* 275 (2019) 807–814.

[58] H. Qin, G. Zhou, J. Yin, L. An, P. Zhao, T. Wang, S. Rao, K. Alireza, J. Yang, L. Zhang, Enhanced photocatalytic performance of g-C₃N₄@Ce-Fe bimetallic oxide with Z-scheme heterojunction for rapid degradation of tetracycline and its photodegradation pathway, *Colloids Surf. A: Physicochem. Eng. Asp.* 652 (2022), 129780.

[59] J. Yang, J. Sun, S. Chen, D. Lan, Z. Li, Z. Li, J. Wei, Z. Yu, H. Zhu, S. Wang, Y. Hou, S-scheme 1 T phase MoSe₂/AgBr heterojunction toward antibiotic degradation: photocatalytic mechanism, degradation pathways, and intermediates toxicity evaluation, *Sep. Purif. Technol.* 290 (2022), 120881.